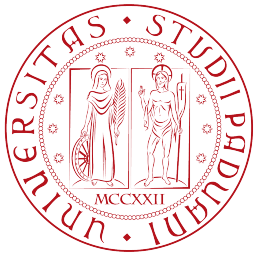

UNIVERSITÀ DEGLI STUDI DI PADOVA

Dipartimento di Fisica e Astronomia "Galileo Galilei"

Master Degree in Physics

Final Dissertation

Laser frequency stabilization for a source of cold Barium atoms

Thesis supervisor

Prof. Dr. Carmelo Mordini

Candidate

Charles Willian Basso

Academic Year 2024/2025

Acknowledgements

Firstly, I would like to deeply thank my father Vilson Basso and my mother Ana Lucia da Silva Basso for the full support during my whole academic journey and for always encouraging me to pursue my aspirations.

I strongly thank Professor Dr. Carmelo Mordini for being the best Supervisor I could have. I learned so many things with him and I am deeply glad that I had the opportunity to be his Master student.

Also, I would like to thank the research fellow Giovanni Merlin of the Quantum Laboratory of the University of Padua for all the support in the laboratory. Additionally, I would like to thank the Quantum Group of the University of Padua, since I learned many things during all the group meetings.

Finally, I would like to thank all the professors that I had in the whole Master's degree in Physics at the University of Padua for all the valuable teachings throughout the course.

This Master Thesis uses an adapted version of the "Data Science MSc Thesis – UniPD" LaTeX template, which was created by Stefano Della Morte and it is available under the Creative Commons Attribution 4.0 International License (CC BY 4.0) at the following web address available online at: "https://www.overleaf.com/latex/templates/data-science-msc-thesis-unipd/wkbhjpbvsytx".

Abstract

The goal of the Master Thesis project is to stabilize the frequency of a 553.7 nm laser in the visible range (green) used in a spectroscopy experimental setup for the energy levels associated with the following atomic transition (related to cooling) of neutral ^{138}Ba atoms: $6s^2\,{}^1S_0 \rightarrow 6s6p\,{}^1P_1$. Additionally, it is used a Hollow Cathode Lamp (HCL) as the source of neutral ^{138}Ba atoms that interact with the laser beam. More specifically, the laser frequency will be stabilized with the use of polarization spectroscopy, which is a Doppler-free technique that consists in the use of a strong pump laser beam, which saturates the population of the excited state, therefore, a weak counter-propagating probe beam faces a reduction in its absorption spectrum, after interacting with the atomic medium, when the detuning is close to zero, characterizing a Lamb dip. Additionally, in polarization spectroscopy, the signal-to-noise ratio is enhanced due to the manipulation of the laser light by using different polarizations, which leads to the coupling between different Zeeman sublevels. As the optical transition of interest is from the S to P sublevels, we can take advantage of polarized light in order to have specific transitions. Finally, another objective of the project is to computationally simulate the overall dynamics of ^{138}Ba atoms in a Magneto-Optical Trap (MOT), in which the atoms are impinged with specific laser lights. The laser-atom interactions, considering specific energy levels that form a cooling cycle, are related to the process of decreasing the motion of the atoms as much as possible, which is the cooling process. After performing the polarization spectroscopy experiment, we were able to observe the Doppler broadening containing the Lamb dip in the absorption spectrum of the probe beam, as well as a Doppler-free signal, which was used to lock the laser frequency in a stable long scan measurement. Finally, we obtained the evolution of the population of the considered energy levels of the ^{138}Ba atom with different numbers of repumping lasers and, also, the optical force in function of the atomic velocity in the central region of a MOT, in order to extract the damping coefficients for each setup configuration for the cooling process.

Contents

1

Introduction

The field of quantum technologies has been growing in the past years due to the potential applications in many fields, such as materials science, quantum chemistry, pharmaceutical production and financing [1]. Also, quantum computing in particular is an innovative approach in order to enhance the computational power with respect to current classical computers, by using intrinsic quantum properties like superposition and entanglement [2].

There are many platforms for quantum computing, such as superconducting circuits, neutral atoms and photonics based, among the others. Quantum computers based on trapped ions are one of the most promising approaches, since they allow precise control of the qubits (ions in this case) with lasers and electric fields [3]. This last approach will be implemented by the Quantum Group of the University of Padua.

In order to have precise control of the qubits, the lasers that are used in order to interact with the energy levels of the ions need to be in a near-resonant regime, which means that the frequency of the laser should be very close to the frequency of the desired atomic transition [4].

In our case, the atom chosen for the laser frequency stabilization is Barium (^{138}Ba) since it is available in high quantities, it has atomic transitions in the visible range and, also, long-lived atomic states [5].

1.1 Sources of noise in laser systems

For the spectroscopy experiment it is necessary to filter the noise related to the laser frequency with a precision of less than 1 MHz. When dealing with lasers, two sources of noise arise, which are the quantum and instrumental ones [6].

The quantum noise is related to the spontaneous decay processes in atomic transitions associated to the mechanism of laser generation, which competes with stimulated emission which is at the basis of lasing mechanism. What happens is that this spontaneous decay is a stochastic process and it is inherently unavoidable due to the quantum nature of the lasing process, leading to dephasing in atom-light interaction [6].

On the other hand, the instrumental noise is associated to technicalities of the experimental apparatus. For instance, mechanical instabilities, thermal fluctuations of the environment, as well as misaligned laser cavities [6].

Therefore, it is notable that a perfectly monochromatic laser is not feasible and, as a consequence, a solution is needed in order to reduce considerably the frequency noise for sub-MHz range. To do so, a spectroscopy technique is a suitable option, since it allows the reduction of the noise through the direct measurement of the targeted atom energy levels. This is done through a feedback loop of the laser light detected after interacting with the ^{138}Ba atoms, which reduces the linewidth around the desired frequency of the laser light [7].

1.2 Structure of the Thesis

The goal of the present work consists in stabilizing the frequency of a laser in the visible range through a suitable spectroscopy technique through its interaction with ^{138}Ba atoms using the atomic transition given by $6s^2\,{}^1S_0 \rightarrow 6s6p\,{}^1P_1$. In addition, computational simulations of the dynamics of the cooling of Ba atoms in a MOT setup will be developed.

In the Section 2 **Theoretical Background** the physics behind the experimental approach is detailed in the context of atom-light interaction. In this sense, the atom will be treated as a quantum object as a 2-level system and, on the other hand, the laser light will be mathematically treated as a classical electromagnetic field that interacts with the atomic medium. Also, regarding the MOT simulation, it will be stated the rate equation that governs the variation of the population of each of the considered levels for the cooling cycle with respect to time. Additionally, the dynamics of the system through the simulation of the force acting on the Ba atoms will also be performed.

Regarding the Section 3 **Experimental Setup**, here it is described the experimental apparatus used in order to perform the spectroscopy technique for stabilizing the laser frequency. Two main experimental parts are emphasized, which is, firstly, the electronics control system in order to provide signal generation, processing and feedback loop and, secondly, the optical components related to both the atomic source and the devices associated to the path of the laser light.

In the end, in the Section 4 **Data Analysis and Results**, fitting procedures associated with the Section 2 **Theoretical Background** are performed to extract important physical parameters regarding the effectiveness of the laser frequency stabilization experiment. Finally, the dynamics of the MOT simulation will also be presented and discussed in this section.

To close the Thesis project, the Section 5 **Conclusions** will focus on a overall look of the work as a whole and will provide prospective indications for further work.

2

Theoretical background

In this section, important reviews regarding the physical theory behind the experiment will be emphasized. Firstly, the atomic structure of the Barium atom and its energy levels will be presented, followed by a semiclassical description of the atom-light interaction and the evolution of an electromagnetic wave in atomic environment. Additionally, a review of saturation spectroscopy will be discussed in order to have a better understanding of the polarization spectroscopy technique, which will be used to stabilize the laser frequency. Finally, the main equations for the simulation of the cooling of Barium atoms in the Magneto-Optical Trap (MOT) will be presented, as well as the physical background associated.

2.1 Review of the Barium atom and the Zeeman sublevels structure

The ^{138}Ba atom is composed of 56 protons and 82 neutrons and it is a neutral and stable alkaline earth element. Also, it has 2 valence electrons and its electronic configuration is [Xe] $6s^2$ [8]. The transitions of the type $6s \rightarrow 6p$ are optically effective and the energy levels of this region with large principal quantum number n are given in the Figure 2.1 below [9].

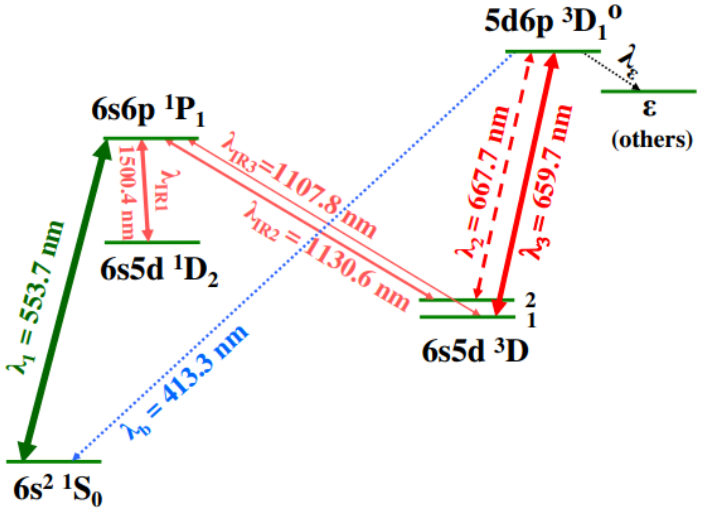

Figure 2.1: Barium energy levels for higher n values. Dashed lines represent spontaneous decays and filled lines are associated to laser induced atomic transitions [9].

Another important distinction associated to the energy levels is related to the Zeeman sublevels. These are characterized by the degeneracy of sublevels with the same orbital angular momentum quantum number l in the absence of an external magnetic field. Since in our case we deal only with transitions $6p$ ($l = 0$) and $6p$ ($l = 1$), we have to distinguish the sublevels associated to the magnetic quantum number m as follows in the next Figure 2.2 [10].

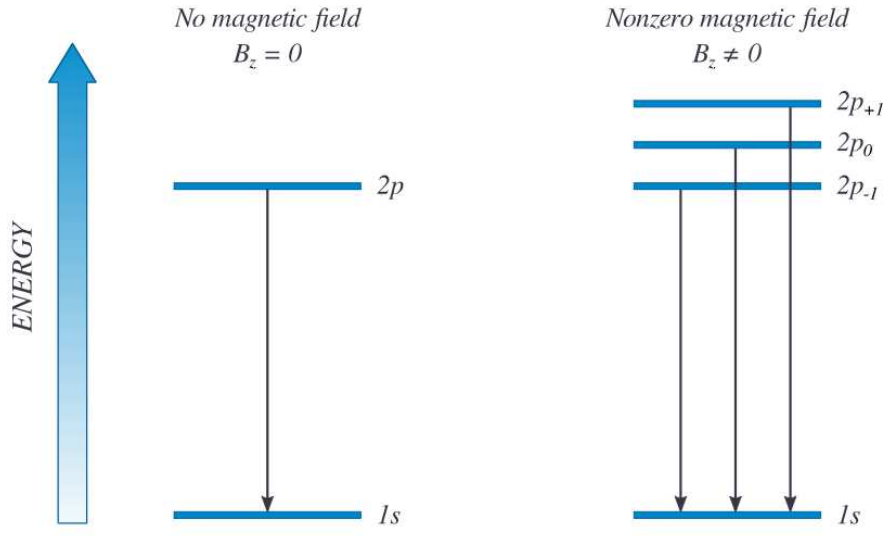

Figure 2.2: Zeeman sublevels for s and p orbitals.

Therefore, for the $6s$ orbital we have only $m = 0$ associated, however, for the $6p$ orbital there are three possible values: $m = -1$, $m = 0$ and $m = +1$. Therefore, if right-handed circularly polarized light excites the electron from the $6s$ to the $6p$ orbital, it goes from $m = 0$ to $m = +1$, however, if left-handed circularly polarized light is used, then the transition will be from $m = 0$ to $m = -1$. Finally, if linearly polarized light is used in this transition, then $\Delta m = 0$ [11].

2.2 Atom-light interaction in 2-level atomic systems

In this section the main considerations and assumptions regarding the atom-light interaction will be detailed in order to describe how the classical laser interacts with the quantum 2-level description of the considered atomic transition. In this whole subsection, the reference [12] is utilized as an inspiration.

2.2.1 Electric dipole approximation

As mentioned before, the laser light is defined here in a classical way, which means that it is characterized by electromagnetic waves. For an atom which is present in an electromagnetic field, the hamiltonian which describes it in the Coulomb Gauge is defined by the Expression 2.1 below [13].

$$H = \sum_i \frac{\left[\vec{p}_i - q_i\vec{A}(\vec{r}_i, t)\right]^2}{2m_i} + q_i\varphi(\vec{r}_i, t) + \sum_{j<i} \frac{q_j q_i}{4\pi\varepsilon_0|\vec{r}_j - \vec{r}_i|} \tag{2.1}$$

In which $\vec{p}_i$ is the linear momentum of the particles (the index i represents both protons and electrons), m_i is the particle mass, q_i the particle charge, ε_0 is the electric permittivity in vacuum, $\varphi(\vec{r}_i, t)$ is the electric potential, $\vec{A}(\vec{r}_i, t)$ is the vector potential and $r_{i,j}$ are the particle positions.

The Coulomb Gauge implies the following condition: $\nabla \cdot \vec{A} = 0$. The first terms are related to free particles in an electromagnetic medium and the last one is associated to the electrostatic interaction between the particles. In classical electrodynamics, it is possible to apply transformations in the field due to gauge invariance. Therefore, for a generalized scalar function χ the following condition applies.

$$\left(\varphi'(\vec{r}, t), \vec{A}'(\vec{r}, t)\right) = \left(\varphi(\vec{r}, t) - \frac{\partial\chi(\vec{r}, t)}{\partial t}, \vec{A}(\vec{r}, t) + \nabla\chi(\vec{r}, t)\right) \tag{2.2}$$

Locating the origin of the coordinate system in the nucleus of the atom and considering the Göppert-Mayer Gauge transformation, the following expression is used for the scalar function χ.

$$\chi(\vec{r},t) = -\vec{r}\cdot\vec{A}(0,t) \tag{2.3}$$

The transformation considering only an electromagnetic wave (absence of charges), we have $\varphi = 0$, and consequently the Göppert-Mayer Gauge gives rise to the following transformation.

$$\left(\varphi'(\vec{r},t), \vec{A}'(\vec{r},t)\right) = \left(\vec{r}\cdot\frac{\partial\vec{A}(0,t)}{\partial t}, \vec{A}(\vec{r},t) - \vec{A}(0,t)\right) \tag{2.4}$$

Now, considering that the wavelength of the electromagnetic wave (which is in the visible range) is much larger than the atom size, the dipole approximation can be used, which consists of approximating the field as uniform in space. This approximation leads to the following relation below, since $\vec{A}(\vec{r},t) \approx \vec{A}(0,t)$.

$$\vec{E}(\vec{r},t) \approx \vec{E}(0,t) \approx -\frac{\partial\vec{A}(0,t)}{\partial t} \tag{2.5}$$

Therefore, given the dipole approximation and the Göppert-Mayer Gauge transformation, the hamiltonian of the atom in the field environment can be written as the following.

$$H = \sum_i \frac{\vec{p}_i^{\,2}}{2m_i} + \sum_{j<i} \frac{q_j q_i}{4\pi\varepsilon_0|\vec{r}_j - \vec{r}_i|} - \vec{d}\cdot\vec{E}(t) \tag{2.6}$$

In the Equation 2.6 above, $\vec{d}$ is the dipole operator and it is given by $\vec{d} = \sum_i q_i\vec{r}_i$. In this case, the hamiltonian is characterized by a purely atomic part H_A and by an atom-light interaction part H_{AL} given by the following Expressions 2.7 and 2.8, respectively.

$$H_A = \sum_i \frac{\vec{p}_i^{\,2}}{2m_i} + \sum_{j<i} \frac{q_j q_i}{4\pi\varepsilon_0|\vec{r}_j - \vec{r}_i|} \tag{2.7}$$

$$H_{AL} = -\vec{d}\cdot\vec{E}(t) \tag{2.8}$$

2.2.2 Atom-light interaction

In this subsection, the interaction of the laser light (treated as a classical object) and the atom (treated as a quantum object) will be presented in an analytical way. This mathematical approach is important in order to understand the underlying mechanisms that are the building blocks for spectroscopy and the whole subsection relies on the reference [14].

In our case, the 2-level system is characterized by two energy levels of the ^{138}Ba atom and the lowest one in energy is denoted as state $|1\rangle$ and the highest state in energy is denoted as $|2\rangle$, which are the ground and excited states, respectively.

These states are eigenstates related to the hamiltonian of the Expression 2.7 and their associated energies of the ground and excited states are $\hbar\omega_1$ and $\hbar\omega_2$, respectively, in which $\hbar$ is the reduced Planck constant and ω_1 and ω_2 are the energies of the ground and excited states divided by $\hbar$, respectively. By defining $\omega_0 = \omega_2 - \omega_1$ and setting the ground state energy as zero, the 2.7 can be written as the following.

$$H_A = \hbar\omega_0 |2\rangle \langle 2| \tag{2.9}$$

Additionally, the H_{AL} can be rewritten in another way, since that the dipole operator due to symmetry properties can be described as the Expression 2.10 below, considering that $\vec{d_{21}} = \vec{d_{12}}^*$ and null diagonal elements.

$$\vec{d} = \vec{d_{12}} |1\rangle \langle 2| + \vec{d_{21}} |2\rangle \langle 1| \tag{2.10}$$

And considering a monochromatic wave with the following expression for the associated electric field.

$$\vec{E} = E_0 \cdot cos(\omega t + \varphi)\, \vec{\varepsilon} \tag{2.11}$$

In which t is the time, φ is a global phase that accounts in the dipole approximation for the uniform spatial dependence, ω is the angular frequency of the light, $\vec{\varepsilon}$ is the polarization vector and E_0 is the wave amplitude. Therefore, the interaction part of the total hamiltonian is given by the Expression 2.12, given that *c.c.* means complex conjugate.

$$H_{AL}(t) = -\vec{\varepsilon} \cdot \vec{d_{12}} E_0 cos(\omega t + \varphi) |1\rangle \langle 2| + c.c. \tag{2.12}$$

2.2.3 Rotating frame transformation

As the total hamiltonian is given by the sum of the time-independent atomic part H_A and the time-dependent one H_{AL}, it is suitable to apply an unitary transformation U given below in order to get rid of this time dependence in a rotating frame.

$$U = \begin{pmatrix} 1 & 0 \\ 0 & e^{i\omega t} \end{pmatrix} \tag{2.13}$$

Moreover, the new hamiltonian in the new rotating frame will be given by the following expression.

$$H' = U(t)H(t)U^{\dagger}(t) + i\hbar\frac{dU(t)}{dt}U^{\dagger}(t) \tag{2.14}$$

Applying this relation 2.14 and defining $\delta = \omega_0 - \omega$ as the detuning between the atomic transition angular frequency and the laser light angular frequency, the total hamiltonian becomes.

$$H = \begin{pmatrix} 0 & -\vec{\varepsilon}\cdot\vec{d_{12}}E_0 cos\left(\omega t + \varphi\right)e^{-i\omega t} \\ -\vec{\varepsilon}\cdot\vec{d_{21}}E_0 cos\left(\omega t + \varphi\right)e^{i\omega t} & \hbar\delta \end{pmatrix} \tag{2.15}$$

Now an important concept is introduced, which is called Rotating Wave Approximation (RWA), which removes the remaining time dependence of the total hamiltonian. This happens because the oscillating terms have a much faster dynamics in comparison with the electric dipole and detuning terms, therefore, the total hamiltonian can be approximated as a time-independent one and it is given by the Expression 2.16.

$$H = \hbar\begin{pmatrix} 0 & \frac{\Omega}{2} \\ \frac{\Omega}{2} & \delta \end{pmatrix} \tag{2.16}$$

The Ω term is called the Rabi frequency and it is associated to the strength of the atom-light interaction and it is given by the Expression 2.17.

$$\Omega = -\frac{\vec{d_{12}}\cdot\vec{\varepsilon}E_0 e^{i\varphi}}{\hbar} \tag{2.17}$$

2.2.4 Open systems

In reality, the atom is not isolated from the external environment, therefore, the evolution of the atomic system is not governed by the Schrödinger equation, which is used for closed quantum systems. Consequently, the use of density matrix formalism is suitable for open systems and the definition of the density matrix operator is given by the Expression 2.18.

$$\rho = \sum_{i,j} \rho_{i,j} \left|i\right\rangle \left\langle j\right| \tag{2.18}$$

This operator of the Expression 2.18 is positive defined, hermitian and its trace is equal to one. This formalism is used in order to describe mixed states and the evolution of the atomic system interacting with the laser light in the environment is given by the Lindblad master equation as follows.

$$\frac{d\rho}{dt} = \frac{1}{i\hbar}[H,\rho] + \mathcal{L}(\rho) \tag{2.19}$$

In which the first term is related to the coherent evolution of the system as a closed system governed by the Schrödinger equation. Additionally, the second term is the Lindblad operator, that describes the incoherent processes and it is directly related to the interaction of the atomic system plus the external environment (bath).

$$\mathcal{L}(\rho) = -\frac{1}{2} \sum_{k} c_k^\dagger c_k \rho + \rho c_k^\dagger c_k - 2 c_k \rho c_k^\dagger \tag{2.20}$$

In which the c_k are known as jump operators and have their construction given by $c_{ij} = \sqrt{\Gamma_{ij}} \left|i\right\rangle \left\langle j\right|$. In this mathematical construction, the jump operators are related to distinct incoherent transitions from the state j to the state i associated to a rate coefficient $\sqrt{\Gamma_{ij}}$ for each transition channel [15].

2.2.5 Spontaneous decay

One of the most important mechanisms of incoherent processes is the spontaneous decay from an excited to a ground state of a 2-level atom. The spontaneous decay rate (linewidth) Γ_{12} from the state $|2\rangle$ to the state $|1\rangle$ is used to determine the associated jump operator, which results in $c_{12} = \sqrt{\Gamma_{12}} \left|1\right\rangle \left\langle 2\right|$.

By applying this jump operator c_{12} in the Linblad operator 2.20, we have the expression that

accounts for the incoherent process of spontaneous decay.

$$\mathcal{L}_{sd}(\rho) = -\frac{1}{2}\Gamma_{12}\left(2\rho_{22}\left|2\right\rangle\left\langle 2\right| + \rho_{12}\left|1\right\rangle\left\langle 2\right| + \rho_{21}\left|2\right\rangle\left\langle 1\right| - 2\rho_{22}\left|1\right\rangle\left\langle 1\right|\right) \tag{2.21}$$

The Lindblad operator 2.21 describes the population imbalance in which the population in the excited state diminishes, causing an increase of the population in the ground state, due to the diagonal terms associated to ρ_{22}. With respect to the non-diagonal terms related to ρ_{12} and ρ_{21}, they are associated to the decoherence phenomena regarding the 2 atomic levels. Also, in the case in which no laser shines the atom, the population of the excited state decreases exponentially and it is governed by the Lindblad master equation 2.19 through the Lindblad operator 2.21.

2.2.6 Dephasing effects

Still considering incoherent phenomena, we also need to take into account dephasing effects, more specifically, two of them. The first one is associated to the rate γ_{las}, that describes how decoherence in the phase of the laser (which comes from the finite linewidth) induces decoherence in the phase of the atomic state and, the second one, is the collisional effect due to the atomic environment of the HCL, which has a rate γ_{coll}. Moreover, the corresponding jump operators for these two phenomena are given by the expression below [14, 16].

$$c_{dph} = \sqrt{2\gamma_{dph}}\left|1\right\rangle\left\langle 1\right| \tag{2.22}$$

In which $\gamma_{dph} = \gamma_{las}$ or $\gamma_{dph} = \gamma_{coll}$ and its corresponding Lindblad operator is given by the Expression 2.23 below.

$$\mathcal{L}_{dph}(\rho) = -\gamma_{dph}\left(\rho_{12}\left|1\right\rangle\left\langle 2\right| + \rho_{21}\left|2\right\rangle\left\langle 1\right|\right) \tag{2.23}$$

In which $\gamma_{dph} = \gamma_{las} + \gamma_{coll}$. Similarly, the Lindblad operator 2.23 affects the coherence of the states by decreasing it through the density matrix.

2.2.7 Optical Bloch Equations

With the use of the Lindblad operators of the Expressions 2.21 and 2.23 and plugging them in the Lindblad master equation 2.19, results in a set of four differential equations corresponding to each of the elements of the density matrix inside the master equation. These equations

are given below.

$$\frac{d\rho_{11}}{dt} = -i\frac{\Omega}{2}(\rho_{21} - \rho_{12}) + \Gamma_{12}\rho_{22} \tag{2.24}$$

$$\frac{d\rho_{22}}{dt} = i\frac{\Omega}{2}(\rho_{21} - \rho_{12}) - \Gamma_{12}\rho_{22} \tag{2.25}$$

$$\frac{d\rho_{12}}{dt} = -i\frac{\Omega}{2}(\rho_{22} - \rho_{11}) - (\gamma_{12} - i\delta)\rho_{12} \tag{2.26}$$

$$\frac{d\rho_{21}}{dt} = i\frac{\Omega}{2}(\rho_{22} - \rho_{11}) - (\gamma_{12} + i\delta)\rho_{21} \tag{2.27}$$

In which γ_{12} is defined as $\gamma_{12} = \gamma_{coll} + \gamma_{las} + \frac{\Gamma_{12}}{2}$. This set of Equations 2.24, 2.25, 2.26 and 2.27 are the so-called Optical Bloch Equations (OBEs) and it is known that the time for convergence is short ($\approx 1\mu s$) and, therefore, we would like to obtain the steady-state solution of the OBEs. In order to do so, the condition $\frac{d\rho}{dt} = 0$ must be imposed, which results in the following solutions.

$$\rho_{11} = 1 - \rho_{22} \tag{2.28}$$

$$\rho_{22} = \frac{\Omega^2}{2}\frac{\gamma_{12}}{\Gamma_{12}}\frac{1}{\delta^2 + \gamma_{12}^2 + \Omega^2\frac{\gamma_{12}}{\Gamma_{12}}} \tag{2.29}$$

$$\rho_{12} = \frac{\Omega}{2}\frac{-\delta + i\gamma_{12}}{\delta^2 + \gamma_{12}^2 + \Omega^2\frac{\gamma_{12}}{\Gamma_{12}}} \tag{2.30}$$

$$\rho_{21} = \rho_{12}^* \tag{2.31}$$

The actual information that we want to extract lies in the solutions 2.29 and 2.30, since the other two solutions are simply the properties of the density matrix operator (trace equals to 1 and positive defined). With a code in Python, it was elaborated the Figure 2.3 containing the functions associated to the solutions of the Expressions 2.29 and 2.30.

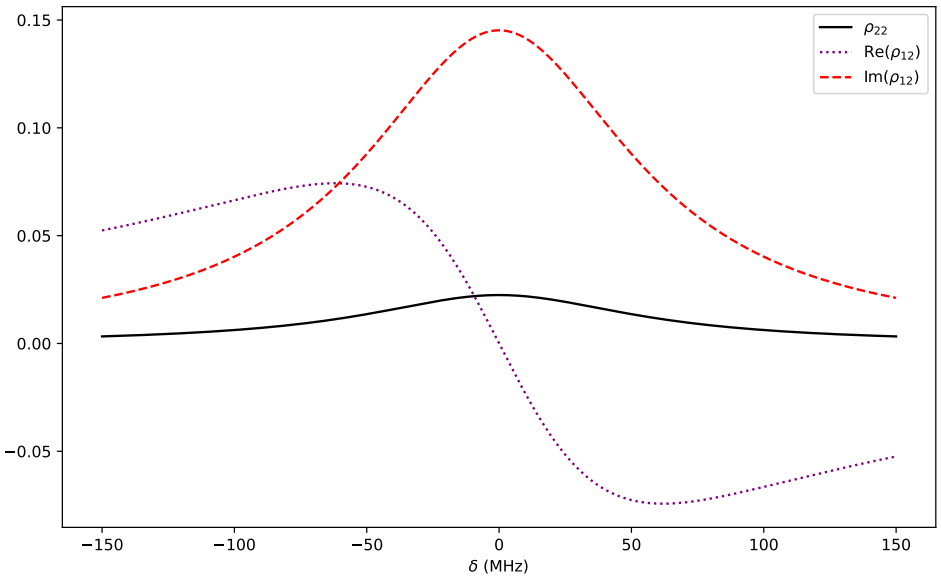

Figure 2.3: ρ_{22}, $Re(\rho_{12})$ and $Im(\rho_{12})$ steady-state solutions of the OBEs in function of the detuning δ. In which the parameters chosen for the simulation are given by: $\gamma_{coll} + \gamma_{las} = 1\,MHz$, $\Omega = 2\pi \cdot 2.9\,MHz$ and $\Gamma_{12} = 2\pi \cdot 18.9\,MHz$ [17].

The Figure 2.3 above shows a dispersive behavior for the $Re(\rho_{12})$ and an absorbing behavior for both the $Im(\rho_{12})$ and ρ_{22} curves, which are also characterized by being centered in $\delta = 0$ and for being Lorentzian functions. This leads to the conclusion that the strength of the coupling between the 2 atomic levels happens when the detuning is the closest possible to zero.

Now we can define the Full Width at Half Maximum (FWHM) in the expression below.

$$\delta_{FWHM} = 2\sqrt{\gamma_{12}^2 + \Omega^2 \frac{\gamma_{12}}{\Gamma_{12}}} = 2\gamma_s \tag{2.32}$$

In which γ_s is the saturation linewidth. From the Expression 2.32 it is noticeable that the natural linewidth, the incoherent effects and, also, the interaction of the laser with the atom end up broadening the linewidth of the transition [18].

2.2.8 Saturation effect

The intensity of the electric field associated to a monochromatic laser is given by the Expression 2.33 below.

$$I = \langle ||\vec{E}(\vec{r},t)||^2 \rangle = \frac{E_0^2}{2} \tag{2.33}$$

From the Expression 2.33 above, we notice that the intensity of the laser light is proportional to the square of the associated electric field amplitude, which means that the intensity is proportional to Ω^2. We define the saturation parameter s in order to have a quantitative way to express the percentage of saturation of the atomic transition and it is given below in the Expression 2.34

$$s = \frac{\Omega^2}{\Gamma_{12}\gamma_{12}} \frac{1}{1+\left(\frac{\delta}{\gamma_{12}}\right)^2} = \frac{s_0}{1+\left(\frac{\delta}{\gamma_{12}}\right)^2} \tag{2.34}$$

In which $s_0 = \frac{I}{I_{sat}}$ is the highest level of saturation, which happens when $\delta = 0$. Moreover, the intensity of saturation is given by the following formula.

$$I_{sat} = \frac{\hbar^2 \Gamma_{12}\gamma_{12}}{2|d_{12}|^2} \tag{2.35}$$

In this way, now it is possible to define the saturation linewidth γ_s in the Expression 2.32 as $\gamma_s = \gamma_{12}\sqrt{1+s_0}$ and the solutions of the OBEs for the steady-state case can be rewritten as the following.

$$\rho_{11} = 1 - \rho_{22} \tag{2.36}$$

$$\rho_{22} = \frac{1}{2}\frac{s}{1+s} \tag{2.37}$$

$$\rho_{12} = \frac{\Omega}{2}\frac{-\delta + i\gamma_{12}}{\delta^2+\gamma_{12}^2}\frac{1}{1+s} \tag{2.38}$$

$$\rho_{21} = \rho_{12}^* \tag{2.39}$$

Given that the population in the ground state is always larger than the population in the excited state, it is noticeable that in the case of a strong saturation regime in which $s >> 1$, the

fraction term $\frac{s}{1+s}$ has a convergence to 1. Therefore, looking at the Expression 2.37 it means that for the strong saturation regime $\rho_{22} \to \frac{1}{2}$ and $\rho_{11} \to \frac{1}{2}$.

2.3 Electromagnetic wave evolution in atomic environment

In the perspective of the electromagnetic wave, the atoms are "seen" as electric dipoles in a way that the atomic medium can be characterized as a polarized environment. Therefore, the electromagnetic wave has its path changed while it interacts with the atoms [14].

The solutions of the OBEs in the steady-state regime were obtained considering the previously discussed rotating frame, therefore, performing an invertion of the basis change 2.13, the density matrix operator can be written as the following, in which $'$ means this alteration of basis, which will be neglected after explicitly showing it.

$$\rho(t) = \begin{pmatrix} \rho'_{11} & \rho'_{12}e^{j\omega t} \\ \rho'_{21}e^{-i\omega t} & \rho'_{22} \end{pmatrix} \tag{2.40}$$

Now we can calculate the expectation value of the dipole moment operator below.

$$\langle \vec{d} \rangle = Tr(\rho \vec{d}) = \rho_{21}\vec{d}_{12}e^{-i\omega t} + c.c. \tag{2.41}$$

Additionally, the dielectric polarization vector $\vec{P}$ can be written as the following.

$$\vec{P} = \frac{\Delta N}{V} \langle \vec{d} \rangle = \varepsilon_0 \chi \vec{E}_0 e^{-i\omega t} + c.c. \tag{2.42}$$

Where $\frac{\Delta N}{V}$ is the population imbalance between the states $|1\rangle$ and $|2\rangle$ and χ is the dielectric susceptibility. In the case where there is no saturation the quantity $\rho_{11} - \rho_{22} \approx 1$ and, consequently, $\frac{\Delta N}{V}$ is characterized by the atomic density itself. So, in this section this will be the considered case for the mathematical treatment, however, in the polarization spectroscopy setup (as it will be seen in a later section) the regime is the saturated one and, then, $\rho_{11} - \rho_{22} \neq 1$.

By relating the Expression 2.42 with the Expression 2.17 of the Rabi frequency and the steady-state solutions of the OBEs, we obtain the dielectric susceptibility χ in function of the

main physical parameters as follows.

$$\chi = -\frac{N}{V}\frac{|d_{12}|^2\rho_{21}}{\hbar\varepsilon_0\Omega} = \frac{N}{V}\frac{|d_{12}|^2}{\hbar\varepsilon_0}\frac{1}{2}\frac{\delta + i\gamma_{12}}{\delta^2 + \gamma_{12}^2 + \Omega^2\frac{\gamma_{12}}{\Gamma_{12}}} = \chi_R + i\chi_I \tag{2.43}$$

In which χ_R is the real part of the dielectric susceptibility χ and χ_I is the imaginary one. Now from Maxwell's relation [14] it can be related to the refractive index n of the atomic medium.

$$\frac{1}{c^2}(1+\chi)\frac{\partial^2\vec{E}}{\partial t^2} = \frac{n^2}{c^2}\frac{\partial^2\vec{E}}{\partial t^2} \tag{2.44}$$

Therefore, the refractive index n can be given in function of the dielectric susceptibility χ and given that χ is small, it can be expanded as the following.

$$n = \sqrt{1+\chi} \approx 1 + \frac{\chi}{2} = n_R + in_I \tag{2.45}$$

Finally, the evolution of the electric field associated to the light beam that interacts with the atomic medium is given by the Expression 2.46.

$$\vec{E}(\vec{r},t) = \vec{\varepsilon}e^{-i\left(\omega t - n_R\frac{\omega}{c}z\right)}e^{-n_I\frac{\omega}{c}z} + c.c. \tag{2.46}$$

Moreover, n_R is associated to the dispersive behavior of the electromagnetic wave, and n_I is related to the absorption processes.

2.4 Review of saturation spectroscopy as a Doppler-free technique

In this section, the foundations of the technique of saturation spectroscopy will be detailed, considering the physical quantities that are extracted.

2.4.1 Doppler effect

The Barium atoms inside the HCL have non-zero velocity due to their natural thermal agitation, therefore, when the electromagnetic wave interacts with them, in their reference frame the wave has an angular frequency given by $\omega - \vec{k}\cdot\vec{v}$. Where $\vec{k}$ is the wavevector defined as $|\vec{k}| = \frac{2\pi}{\lambda}$, in which λ is the wavelength of the light and $\vec{v}$ is the velocity of the atom.

Furthermore, the mathematical relations obtained so far are still valid with the condition that this effect is accounted, in which the detuning $\delta(\vec{v})$ will be given in function of the velocity of the atoms, as given below.

$$\delta(\vec{v}) = \delta + \vec{k} \cdot \vec{v} \tag{2.47}$$

This relation 2.47 implies that in the interaction of the laser light with the atom as a 2-level system, in order to couple two energy levels, it will only occur when the deviation of the detuning due to the Doppler effect is smaller than the associated linewidth of the transition. Consequently, for every equation in which the detuning δ appears, it must be substituted by the relation 2.47 to incorporate the Doppler effect. In the Expression 2.48 this relation is detailed and in 2.49 it is presented the Maxwell-Boltzmann distribution probability $\omega(v_z)$ of the velocities of the atoms along the z direction, which is assumed as the direction of the propagation of the electromagnetic field [14].

$$|\delta + \vec{k} \cdot \vec{v}| < \gamma_s \tag{2.48}$$

$$\omega(v_z) = \frac{1}{\sqrt{2\pi} v_{th}} e^{-\frac{v_z^2}{2v_{th}^2}} \tag{2.49}$$

In which $v_{th} = \sqrt{\frac{k_b T}{m}}$, T is the temperature in Kelvin, m is the mass of the atom and k_b is the Boltzmann constant. In this case, it is possible to write the population density for each level with the following expression.

$$N_i(v_z) dv_z = \rho_{ii}(v_z) \omega(v_z) dv_z \tag{2.50}$$

Therefore, by using the Expressions 2.28, 2.29, 2.47, 2.48, 2.49, 2.50, it was possible to construct the corresponding figures containing the population density for the ground and excited states, respectively, in function of the velocity of the atoms for different values of the detuning $\delta(v_z)$. These Figures 2.4 and 2.5 are presented below.

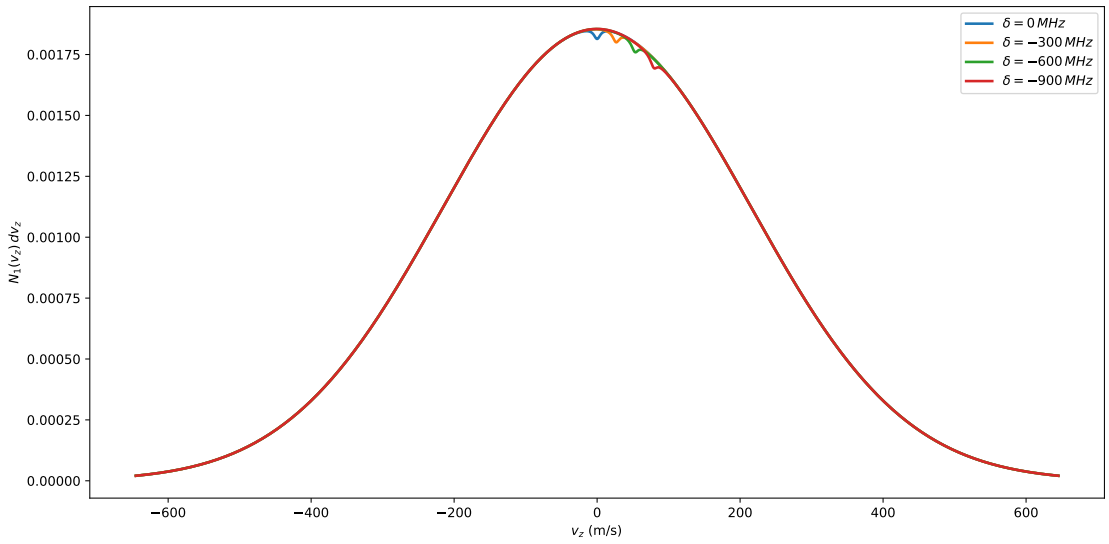

Figure 2.4: Population density of the ground state $|1\rangle$ in function of the velocity of the atoms for different values of the detuning $\delta(v_z)$. In which the parameters chosen for the simulation are given by: $\gamma_{coll} + \gamma_{las} = 1\,MHz$, $\Omega = 2\pi \cdot 2.9\,MHz$, $\Gamma_{12} = 2\pi \cdot 18.9\,MHz$, $T = 500\,K$, $\gamma_s = 10MHz$ and $\lambda = 553.7\,nm$ [17].

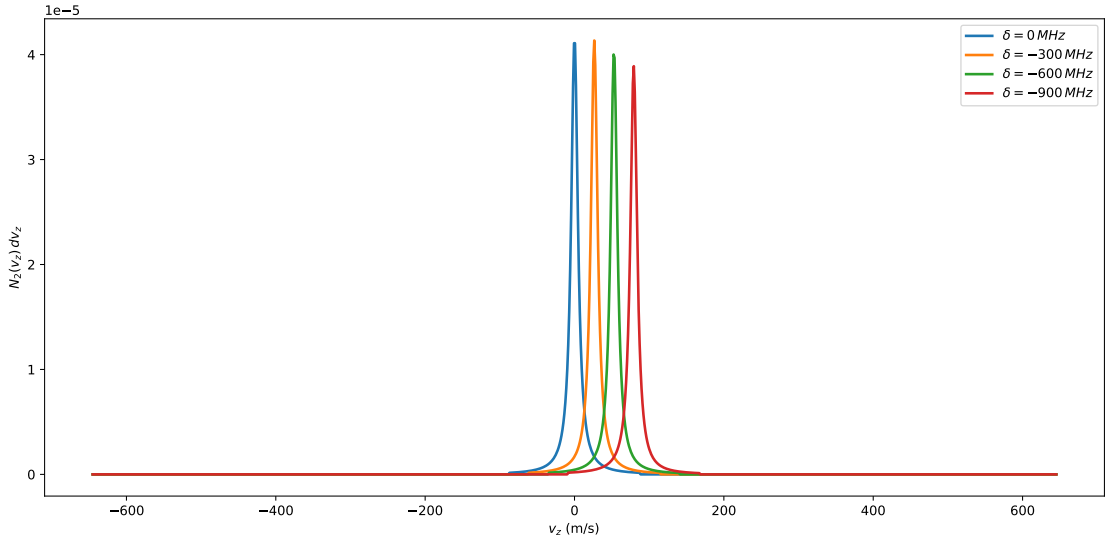

Figure 2.5: Population density of the excited state $|2\rangle$ in function of the velocity of the atoms for different values of the detuning $\delta(v_z)$. In which the parameters chosen for the simulation are given by: $\gamma_{coll} + \gamma_{las} = 1\,MHz$, $\Omega = 2\pi \cdot 2.9\,MHz$, $\Gamma_{12} = 2\pi \cdot 18.9\,MHz$, $T = 500\,K$, $\gamma_s = 10MHz$ and $\lambda = 553.7\,nm$ [17].

It is clear from the Figures 2.4 and 2.5 that the interaction of the laser with the atom causes the depletion of the population in the ground state and it populates the excited state under

the condition of the Expression 2.48, which creates a Bennet hole in the ground state $|1\rangle$ and a Bennet peak in the excited state $|2\rangle$ [19].

Moreover, the dielectric susceptibility χ is also affected by the Doppler broadening as expected, therefore, it is necessary to integrate the previously discussed one 2.43 by weighting it by the Maxwell-Boltzmann relation 2.49 as follows.

$$\chi_{Doppler} = \int \chi(\omega - kv_z)\omega(v_z)dv_z \tag{2.51}$$

The absorption coefficient is associated with the imaginary part of the dielectric susceptibility, which is characterized as the convolution of Gaussian and Lorentzian functions. But in case of the Barium atoms in the HCL, the condition $kv_{th} >> \gamma_s$ applies, due to the higher thermal velocity of the atoms.

Under this condition, the Lorentzian part of the imaginary part of the dielectric susceptibility can be approximated as a Dirac delta function as follows.

$$\chi_{Doppler_I} = \frac{N}{V}\frac{|d_{12}|^2}{\hbar\varepsilon_0}\frac{\pi\gamma_{12}}{2\gamma_s}\int \frac{dv_z}{\sqrt{2\pi}v_{th}} e^{-\frac{v_z^2}{2v_{th}^2}} \frac{1}{\pi}\frac{\gamma_s}{(\delta + kv_z) + \gamma_s^2} \tag{2.52}$$

$$\chi_{Doppler_I} = \frac{N}{V}\frac{|d_{12}|^2}{\hbar\varepsilon_0}\frac{\pi\gamma_{12}}{2\gamma_s}\int \frac{dv_z}{\sqrt{2\pi}v_{th}} e^{-\frac{v_z^2}{2v_{th}^2}} \delta_{Dir}(\delta + kv_z) \tag{2.53}$$

$$\chi_{Doppler_I} = \frac{N}{V}\frac{|d_{12}|^2}{\hbar\varepsilon_0}\frac{\pi\gamma_{12}}{2\gamma_s}\frac{1}{\sqrt{2\pi}kv_{th}} e^{-\frac{\delta^2}{2(kv_{th})^2}} \tag{2.54}$$

Therefore, the approximation above of the Expression 2.54 gives a Gaussian function with standard deviation $\sigma = kv_{th}$. Also, in the following figure there is a representation of the ρ_{22}, $Re(\rho_{12})$ and $Im(\rho_{12})$ curves in function of the detuning, as well as the Gaussian simulation curve from the Expression 2.54 for both the ρ_{22} and $Im(\rho_{12})$ functions.

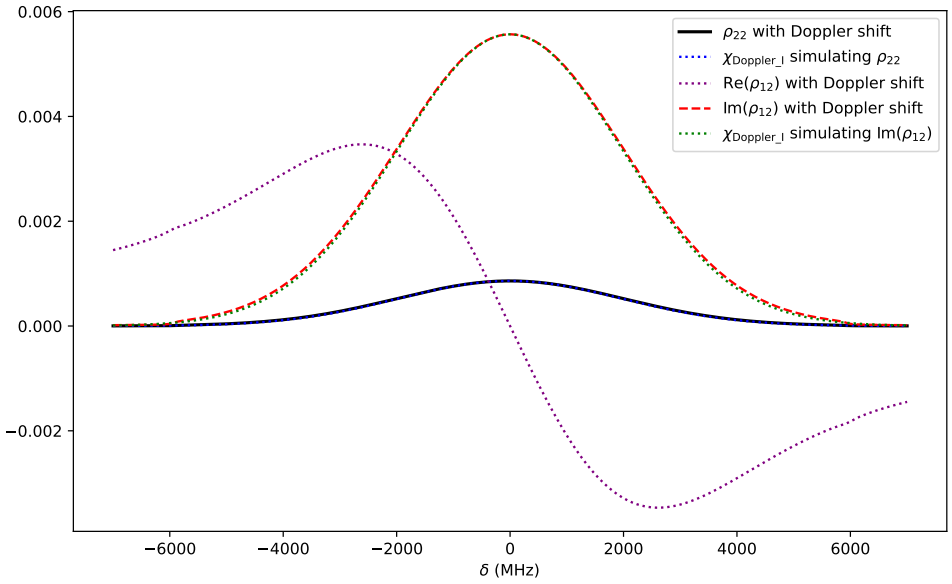

Figure 2.6: ρ_{22}, $Re(\rho_{12})$ and $Im(\rho_{12})$ steady-state solutions of the OBEs in function of the detuning δ considering the Doppler effect. In which the parameters chosen for the simulation are given by: $\gamma_{coll} + \gamma_{las} = 1\,MHz$, $\Omega = 2\pi \cdot 2.9\,MHz$ and $\Gamma_{12} = 2\pi \cdot 18.9\,MHz$ [17]. Also, in the graph there is also the normalized Gaussian simulation from the Expression 2.54 for both the ρ_{22} and $Im(\rho_{12})$ functions. The remaining parameters used are: $T = 500\,K$, $N/V = 1$, $d_{12} = 1 \times 10^{-29}\,C.m$ and $\gamma_s = 10\,MHz$.

2.4.2 Doppler-free saturation spectroscopy

Although the technique used for locking the laser frequency of the atomic transition of a 2-level system is the polarization spectroscopy, it is important to describe before the saturation spectroscopy, which has a similar working principle and it helps to explain the concepts of Doppler-free and Lamb dip effects.

The working principle of the saturation spectroscopy consists of shining the atomic environment with a strong pump beam and, in the opposite direction, it is impinged a weak counter-propagating probe beam with the same frequency of the pump laser. Assuming that the pump beam is directed in the z direction, it couples with the atom for a 2-level transition in the velocity dispersion associated to $-\delta - \gamma_s < kv < -\delta + \gamma_s$.

As the pump beam is the strong one, it creates a Bennet hole in this range of velocities, leading to an imbalance of the population of the 2 states given by the next figure.

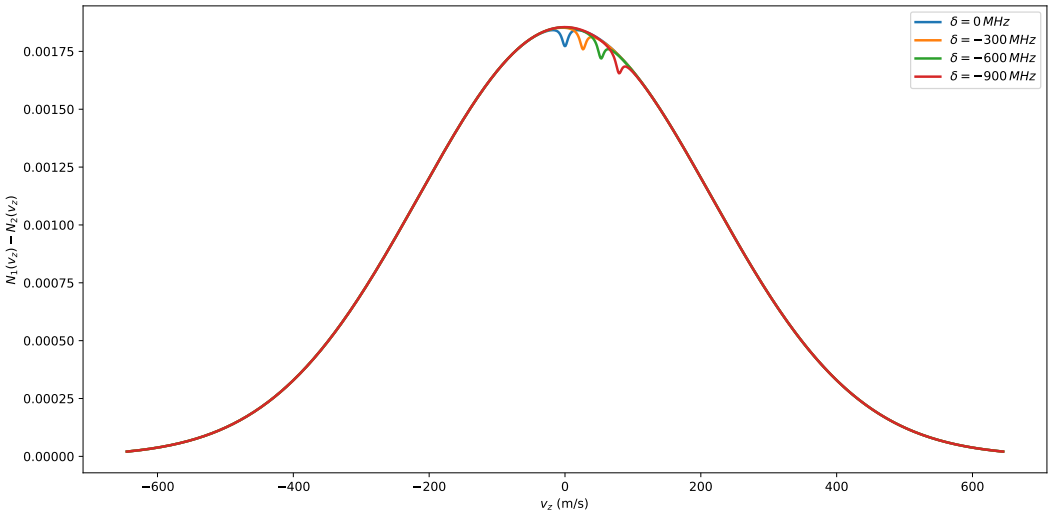

Figure 2.7: Population density difference in function of the velocity of the atoms for different values of the detuning $\delta(v_z)$. In which the parameters chosen for the simulation are given by: $\gamma_{coll} + \gamma_{las} = 1\,MHz$, $\Omega = 2\pi \cdot 2.9\,MHz$, $\Gamma_{12} = 2\pi \cdot 18.9\,MHz$, $T = 500\,K$ and $\lambda = 553.7\,nm$ [17].

Additionally, the weak probe beam does not affect the population imbalance since it does not saturate it, therefore, the population imbalance is essentially determined by the pump beam. Also, the imaginary part of the ρ_{12} component of the density matrix in function of the velocity of the atoms associated to the probe beam is given in the next figure.

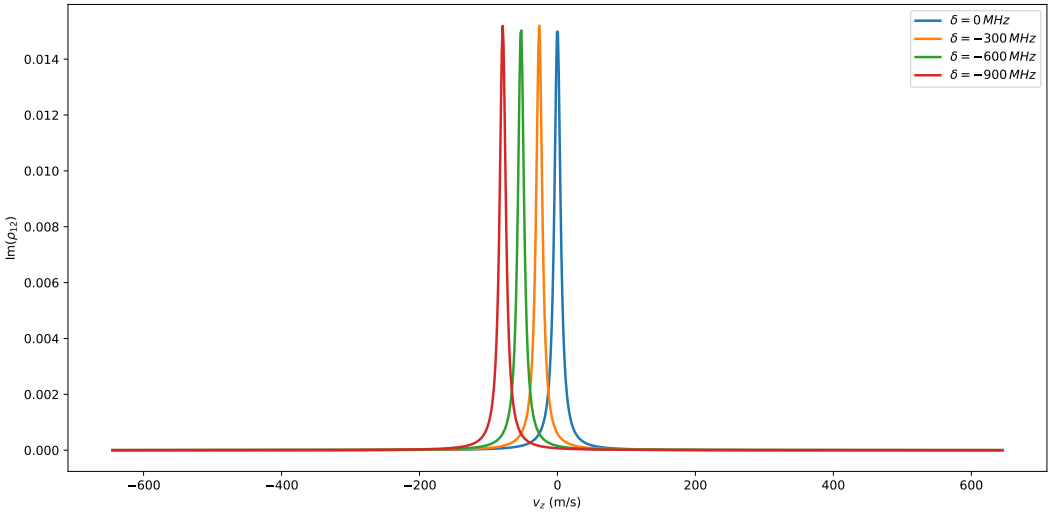

Figure 2.8: $Im(\rho_{12})$ in function of the velocity of the atoms for different values of the detuning $\delta(v_z)$. In which the parameters chosen for the simulation are given by: $\gamma_{coll} + \gamma_{las} = 1\,MHz$, $\Omega_{probe} = \Omega/10 = 2\pi \cdot 0.29\,MHz$, $\Gamma_{12} = 2\pi \cdot 18.9\,MHz$, $T = 500\,K$ and $\lambda = 553.7\,nm$ [17].

Similarly, the probe beam has a range of interaction in the interval $\delta - \gamma_{12} < kv < \delta + \gamma_{12}$ and in saturation spectroscopy, the measurement occurs in the probe beam specifically. The technique is called Doppler-free because as it is demonstrated in the Figures 2.7 and 2.8 above, the hole of the population imbalance and the peak of the imaginary part of ρ_{12}, respectively, only match in the condition $\delta \approx 0$. An other way to understand it is by noticing that this condition happens when the velocity of the interacting atoms in the z direction tends to zero (Doppler-free).

Furthermore, the imaginary part of the refractive index n is given in the following expression.

$$Im(n) \propto \int \Delta N(v_z) \cdot Im(\rho_{12}) dv_z \tag{2.55}$$

By integrating the Expression 2.55 above numerically in Python, the following figure in which the absorption intensity in function of the detuning is presented.

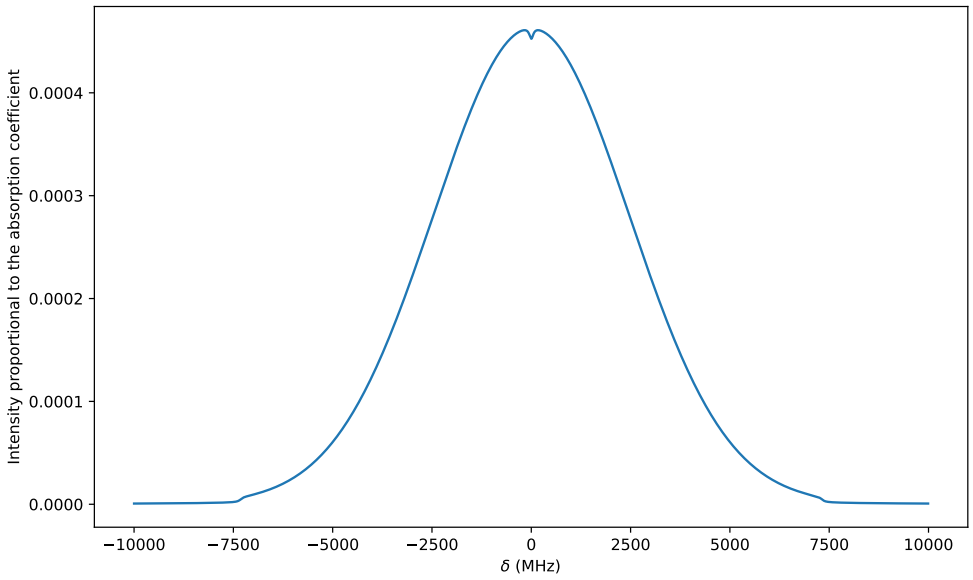

Figure 2.9: Intensity proportional to the absorption coefficient in function of the detuning. In which the parameters chosen for the simulation are given by: $\gamma_{coll} + \gamma_{las} = 1\,MHz$, $\Omega = 2\pi \cdot 2.9\,MHz$, $\Omega_{probe} = \Omega/10 = 2\pi \cdot 0.29\,MHz$, $\Gamma_{12} = 2\pi \cdot 18.9\,MHz$, $T = 500\,K$ and $\lambda = 553.7\,nm$ [17].

From the figure above, it is noticeable that in $\delta \approx 0$, the absorption coefficient has a decrease in intensity, which is called Lamb dip [19].

2.5 Laser frequency stabilization with polarization spectroscopy

In the present work, the laser frequency is stabilized with the use of polarization spectroscopy, which is a Doppler-free technique that uses the same principles of saturation spectroscopy, meaning that a strong pump laser beam saturates the population in the excited state, therefore, a weak counter-propagating probe beam faces a reduction in its absorption spectrum after interacting with the atomic medium when $\delta \approx 0$, which consists in a Lamb dip.

However, in polarization spectroscopy, the signal-to-noise ratio is enhanced due to the manipulation of the laser light by using different polarizations, which leads to the coupling between different Zeeman sublevels [19, 20]. As the optical transition of interest is from the S to P sublevels, we can take advantage of polarized light in order to have specific transitions as detailed in the following figure.

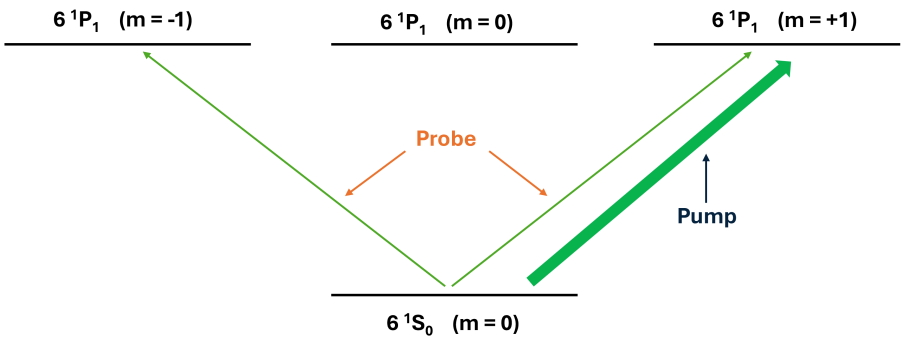

Figure 2.10: Zeeman sublevels schematics for the transitions from the S to P levels and indication of the pump and probe couplings for different sublevels, which are used in polarization spectroscopy.

As seen in the figure above, the technique of polarization spectroscopy uses a circularly right polarized pump beam and, on the other hand, the probe beam consists of a linearly polarized light along the x direction, in which both lasers move in the z direction as defined in the previews section in opposite paths. Therefore, the probe beam has 2 components that are analyzed in order to improve the signal-to-noise ratio in comparison to a standard saturation spectroscopy technique. The electric field of the pump and probe beams, respectively, are given by

the following expressions.

$$\vec{E} = E_0 \vec{\varepsilon_+} \tag{2.56}$$

$$\vec{E} = \frac{E_0}{\sqrt{2}} (\vec{\varepsilon_-} - \vec{\varepsilon_+}) \tag{2.57}$$

In which the polarization vectors associated to the circular polarization can be expressed in function of the ones associated to the cartesian coordinates given by the following expression.

$$\vec{\varepsilon_\pm} = \mp \frac{\vec{\varepsilon_x} \pm i\vec{\varepsilon_y}}{\sqrt{2}} \tag{2.58}$$

Moreover, through the detection of the two components of the probe beam, it is possible to relate the difference in intensity of the two signals with important physical quantities in the following expression below obtained in details in the **Appendix A**.

$$\Delta I = \frac{E_0^2}{2} e^{-2Im(n_{tot}+\omega_{tot})\frac{\omega L}{c}} \frac{\omega L}{c} Re(\Delta n) \tag{2.59}$$

In which L is the HCL's length and $\frac{E_0^2}{2}$ is the intensity of the probe beam before crossing the atomic medium. Moreover, given that n_+ and n_- are the refractive indexes as seen by the circularly right and left polarized probe beam when it interacts with the atomic medium, respectively, and, also, ω_+ and ω_- are the equivalent with respect to the interaction of the probe beam components with the glass of the HCL. The differences of these quantities are defined as $\Delta n = n_+ - n_-$ and $\Delta\omega = \omega_+ - \omega_-$ and n_{tot} and w_{tot} are the simple arithmetic average of these quantities, respectively.

Therefore, the difference of the real part of the refractive indexes is related to the signal processing in order to perform the feedback loop of the laser frequency. The relation between this quantity with the previously discussed physical parameters is given in the following expression derived in the **Appendix B**.

$$Re(\Delta n) = -\frac{N}{V} \frac{|d_{12}|^2}{8\hbar\varepsilon_0} \frac{\pi\gamma_{12}\Omega^2}{2\Gamma_{12}\sqrt{2\pi}kv_{th}\gamma_s} e^{-\frac{\delta^2}{2(kv_{th})^2}} \frac{\delta}{\delta^2 + \frac{(\gamma_{12}+\gamma_s)^2}{4}} \tag{2.60}$$

This expression has a Gaussian term associated to the exponential factor which has a slower dynamics when compared to the Lorentzian part and it is clear that it is Doppler-free with FWHM given by $\gamma_{12} + \gamma_s$.

For visualizing the Expression 2.60, it follows a graph in which the $Re(\Delta n)$ in function of the detuning δ for different values of Ω_{pump} is presented.

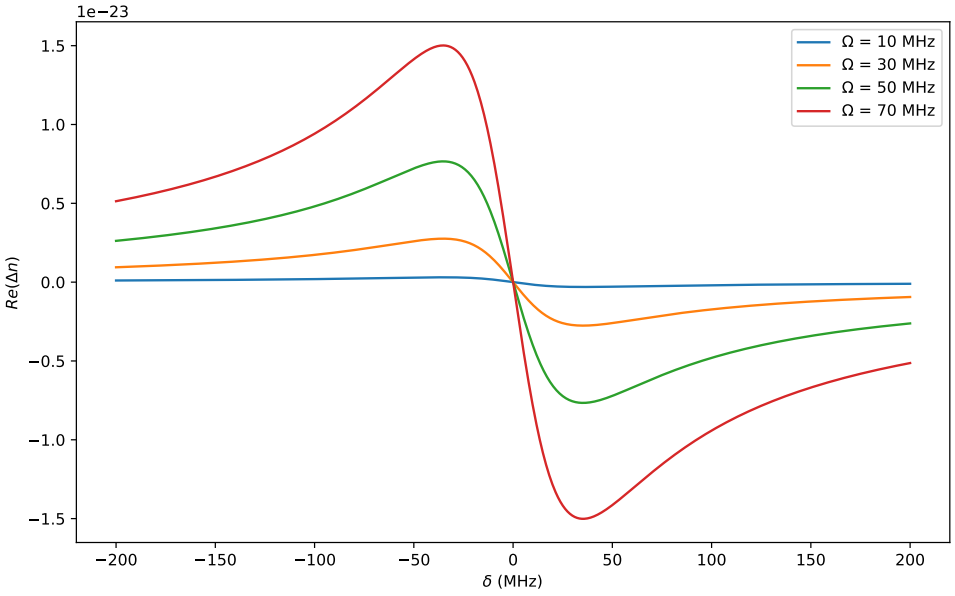

Figure 2.11: $Re(\Delta n)$ in function of the detuning for different values of Ω_{pump}. In which the parameters chosen for the simulation are given by: $\gamma_{coll} + \gamma_{las} = 1\,MHz$, $\Omega = 2\pi \cdot 2.9\,MHz$, $\gamma_s = 10\,MHz$, $\Gamma_{12} = 2\pi \cdot 18.9\,MHz$, $d_{12} = 1 \times 10^{-29}\,C.m$, $N/V = 1$, $T = 500\,K$ and $\lambda = 553.7\,nm$ [17].

From the figure above, it is noticeable that when Ω_{pump} increases, the amplitude of the dispersion curves increases as well and they also get more steep. Additionally, all the four curves overlap at $\delta \approx 0$.

In our case, it will be used an Acousto-Optic Modulator (AOM) that will be explained in details in the next section. This device allows the control of the passage/blocking of the pump beam, therefore, a correction must be added into the Expression 2.60 by adding $\frac{\delta_{AOM}}{2}$ into the detuning terms as follows.

$$Re(\Delta n) = -\frac{N}{V}\frac{|d_{12}|^2}{8\hbar\varepsilon_0}\frac{\pi\gamma_{12}\Omega^2}{2\Gamma_{12}\sqrt{2\pi}kv_{th}\gamma_s}e^{-\frac{\left(\delta+\frac{\delta_{AOM}}{2}\right)^2}{2(kv_{th})^2}}\frac{\left(\delta+\frac{\delta_{AOM}}{2}\right)}{\left(\delta+\frac{\delta_{AOM}}{2}\right)^2+\frac{(\gamma_{12}+\gamma_s)^2}{4}} \tag{2.61}$$

In which δ_{AOM} is the frequency of the signal that controls the AOM behavior.

2.6 Cooling of Barium atoms in a Magneto-Optical Trap (MOT)

In the field of atomic physics, in which a high precision measurement is necessary, such as in trapped ion quantum platforms, the use a Magneto-Optical Trap (MOT) is a standard method. It consists in using a chamber kept in ultra-high vacuum in which a differential magnetic field along a specific direction acts on the atomic source (Ba atoms in this case). In this configuration, the main part of the MOT is the interaction of the laser beams with specific atomic transitions, considering a few energy levels. These levels form the cooling cycle through the exchange of momentum between the photons and the Ba atoms [9].

The energy levels that are considered in the present work are the following: $6s^2\,{}^1S_0$, $6s6p\,{}^1P_1$, $6s5d\,{}^1D_2$, $6s5d\,{}^3D_2$ and $6s5d\,{}^3D_1$. These levels and their associated wavelengths for the atomic transitions are illustrated in the Figure 2.1.

2.6.1 Rate equation

In order to simulate the variation of the population of electrons in each of the considered atomic levels taking into account the incident laser beams, it is used the following rate equation [21].

$$\frac{d}{dt}N_i = \sum_{j>i}\Gamma_{ji}N_j - \sum_{j<i}\Gamma_{ij}N_i - \frac{N_i}{\tau_{\text{Loss}}} + \sum_{l,j}\frac{\pi^2c^3}{\hbar\omega_{ij}^3}\frac{I_l}{2\pi c}\times\frac{\Gamma_{ij}^2}{(\omega_{ij}-\omega_l)^2+\frac{\Gamma_{ij}^2}{4}}\left(N_j - \frac{2J_j+1}{2J_i+1}N_i\right) \tag{2.62}$$

This Equation 2.62 describes the population dynamics for each level in which a monochromatic laser induces a transition from the level i to j. In which N_i is the population of the level i, N_j is the population of the level j, Γ_{ij} is the linewidth for spontaneous emission from the more energetic to the less energetic level, τ_{loss} is associated to the time that uncooled atoms leave the MOT region, ω_{ij} and ω_l are the angular frequencies associated to the energy difference between the atomic levels and of the laser beam, respectively. Finally, I_l is the laser intensity and the index l refers to the lasers associated to each transition. When there are more than one level where it is possible to decay, the linewidth of the higher state is the sum of all decay rates. Additionally, $J_{i,j}$ are the total angular momentum of the respective levels [21].

The first term of the Equation 2.62 is characterized by the spontaneous emission from a state j which is more energetic than the considered state i, the second term is the equivalent but from the state i to a less energetic state j. Additionally, the third term is related to the losses of atoms

from the MOT region and the fourth term is related to the laser-induced absorption process, which takes into account the degeneracies of each level as well [21].

2.6.2 Force equation in a MOT setup

For the simulation of the dynamics of Barium atoms in a MOT, it is used a rate force equation [22], which is given by the following expression.

$$\vec{F} = \sum_{l} \frac{\hbar \vec{k_l}}{2} \sum_{i,j} R_{ij}^{l} \tag{2.63}$$

In which the index l corresponds to each laser beam, $\vec{k_l}$ is their corresponding wavevector and R_{ij}^{l} is the scattering rate between the states i and j.

Moreover, the scattering rate is defined by the last term of the Expression 2.62 and it is shown explicitly below.

$$R_{ij}^{l} = \sum_{l,j} \frac{\pi^2 c^3}{\hbar \omega_{ij}^3} \frac{I_l}{2\pi c} \times \frac{\Gamma_{ij}^2}{(\omega_{ij} - \omega_l)^2 + \frac{\Gamma_{ij}^2}{4}} \left(N_j - \frac{2J_j + 1}{2J_i + 1} N_i \right) \tag{2.64}$$

Additionally, in a $1D$ MOT, considering 2 counter-propagating lasers with the frequency of the main transition with $\delta_{12} = \omega_{12} - \omega_l < 0$ and considering the Doppler effect due to the velocity of the Ba atoms, the expression that relates the optical force on the atoms in function of their velocities is given by the following expression that uses the Expression 2.63 by using the last term of the Equation 2.62 as the scattering rate R_{ij}^{l}.

$$F(v) = -\frac{\hbar k}{2} \frac{\Gamma_{21} \pi c^2 I_{12}}{2\hbar \omega_{12}^3} \left(N_2 - \frac{2J_2 + 1}{2J_1 + 1} N_1 \right) \left(\frac{\Gamma_{21}}{(\delta_{12} - kv)^2 + \left(\frac{\Gamma_{21}}{2}\right)^2} - \frac{\Gamma_{21}}{(\delta_{12} + kv)^2 + \left(\frac{\Gamma_{21}}{2}\right)^2} \right) \tag{2.65}$$

In the expression above, N_1 and N_2 are the populations of the ground and excited states, respectively, and this equation can be used to determine the damping coefficient α in the linear regime for low velocities, since for small velocities the force is linearly related to the velocity as $F(v) = -\alpha v$ [23].

3
Experimental setup

The experimental setup consists of the electronics control part with the use of a micro-controller (RedPitaya platform), as well as the optical table part. This whole setup is the experimental apparatus in order to perform a polarization spectroscopy technique for the lock-in of the laser. The schematics of the experiment is presented in the next figure.

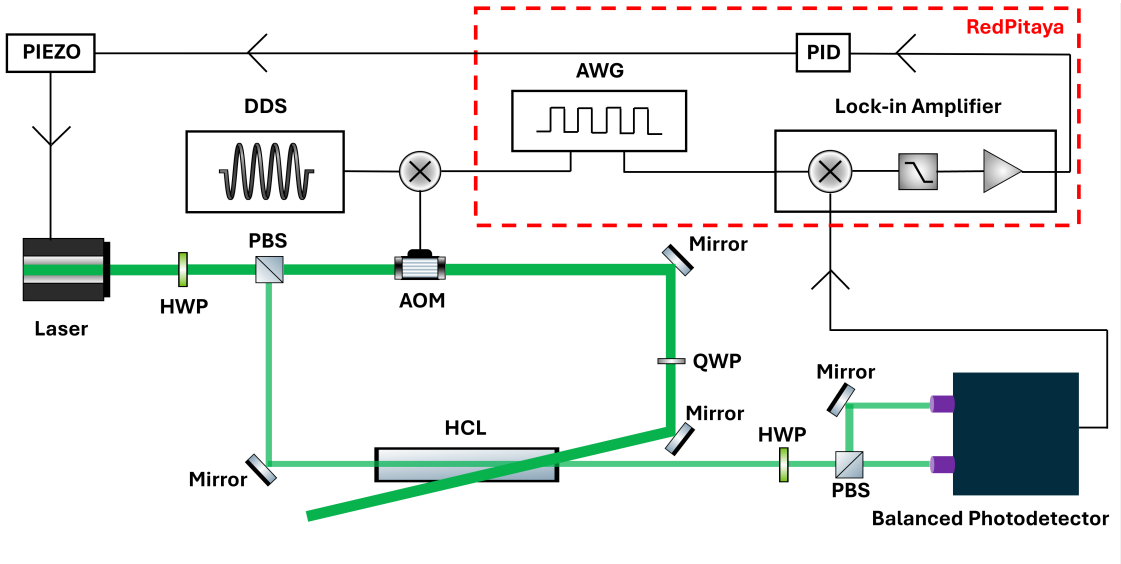

Figure 3.1: Illustration of the polarization spectroscopy setup for the laser lock-in, which was designed by using the *ComponentLibrary* drawings [24]. ComponentLibrary by Alexander Franzen is licensed under a Creative Commons Attribution-NonCommercial 3.0 Unported License.

In the Figure 3.1, DDS means Direct Digital Synthesizer, AWG is Arbitrary Waveform Generator, HWP means Half-Wave Plate, PBS is Polarizing Beam Splitter, AOM means Acousto-Optic Modulator, QWP is Quarter-Wave Plate and HCL is Hollow Cathode Lamp. Additionally, the thicker beam is the pump one and the thinner is the probe one.

3.1 Electronics control

The electronics control of the polarization spectroscopy setup has three main parts, signal generation, signal detection and signal processing. The signal detection is made by a balanced photodetector, which receives the intensities of the laser beam I_x and I_y and subtracts them in order to send it to the lock-in amplifier. Additionally, the functions of the AWG and lock-in amplifier are all performed by a RedPitaya platform [25] and the DDS function is made by a Radio Frequency (RF) signal generator (*Hewlett Packard: Model 8648B*). An illustration of the RedPitaya platform is presented in the next figure.

Moreover, the RedPitaya is also responsible for the PID control of the laser frequency stabilization in the feedback loop, as shown in the Figure 3.1.

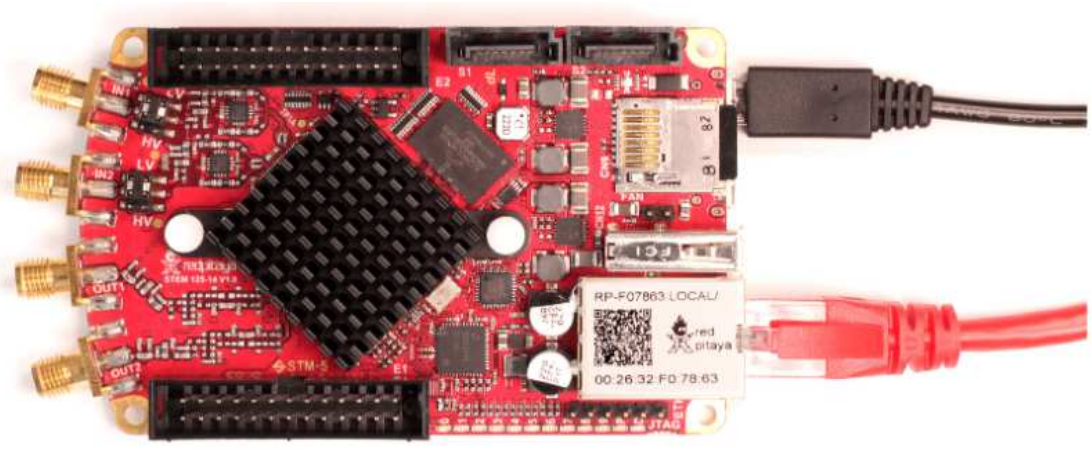

Figure 3.2: Illustration of the RedPitaya platform [25].

The RedPitaya is a device that has an advanced microprocessor that is programable through a web interface, in which it connects through the internet to a server. This device is suitable for generating signals, receive signals and, also, treat the incoming signals, all in one single device, as it will be detailed in the subsection below.

3.1.1 RedPitaya as signal generator and lock-in amplifier

The Redpitaya can generate a square shaped signal of KHz range as a AWG. Furthermore, the lock-in amplifier, which is also performed by the RedPitaya platform, consists in getting a square wave signal from the AWG with angular frequency ω_{ref} and creating a sinusoidal signal with the same frequency as a reference. Additionally, the incoming signal from the balanced photodetector with frequency ω_{sig}, is then multiplied by the reference signal, resulting in the output signal given by the following Expression [26].

$$U_{output}(t) = \frac{1}{2} V_{ref} V_{sig} \left[\cos\left((\omega_{ref} - \omega_{sig})t + (\theta_{ref} - \theta_{sig})\right) - \cos\left((\omega_{ref} + \omega_{sig})t + (\theta_{ref} + \theta_{sig})\right)\right] \tag{3.1}$$

In which V_{ref} and V_{sig} are the amplitudes of the reference and incoming signals, respectively. Also, ω_{ref} and ω_{sig} are the respective phases of the signals and t is the time. As the goal is the DC part of the Expression 3.1, the signal is chopped with the reference one and, as a consequence, a low-pass filter acts for keeping the low frequency part of the signal and, then, it is amplified. In the end, the lock-in amplifier essentially acts as a band-pass filter in order to exclude the frequencies that are not close to the one of the reference signal, which has the order of magnitude in frequency of kHz, in our case.

3.2 Main optical components

In order to perform the polarization spectroscopy experiment, a collection of optical components are used in order to manipulate the laser beams, as well as setting their direction of propagation. Among all the optical components, one that deserves a separate description is the Acousto-Optic Modulator (AOM) which acts as an electronic chopper for the laser beam. Additionally, a more detailed description of the Hollow Cathode Lamp (HCL) used to generate the low pressure vapor of neutral Barium atoms will be performed in this subsection. Furthermore, the working mechanism of the laser used in the experiments will also be detailed.

3.2.1 Acousto-Optic Modulator

The AOM, which in our case is the *Gooch & Housego - Model:* 3080 − 125, is an electronics device which controls the passage of the laser beam as a chopper. Basically, this device is made of a material in which its refractive index can be controlled through the application of a radio-frequency signal (RF) to the AOM driver. When the laser beam passes through the AOM, if the RF signal is not being applied, the beam gets blocked, otherwise, it passes through the

AOM with an angle characteristic of the order of the Bragg diffraction due to the light-phonon coupling [27]. A schematics of the Bragg diffraction in an AOM is shown in the figure below.

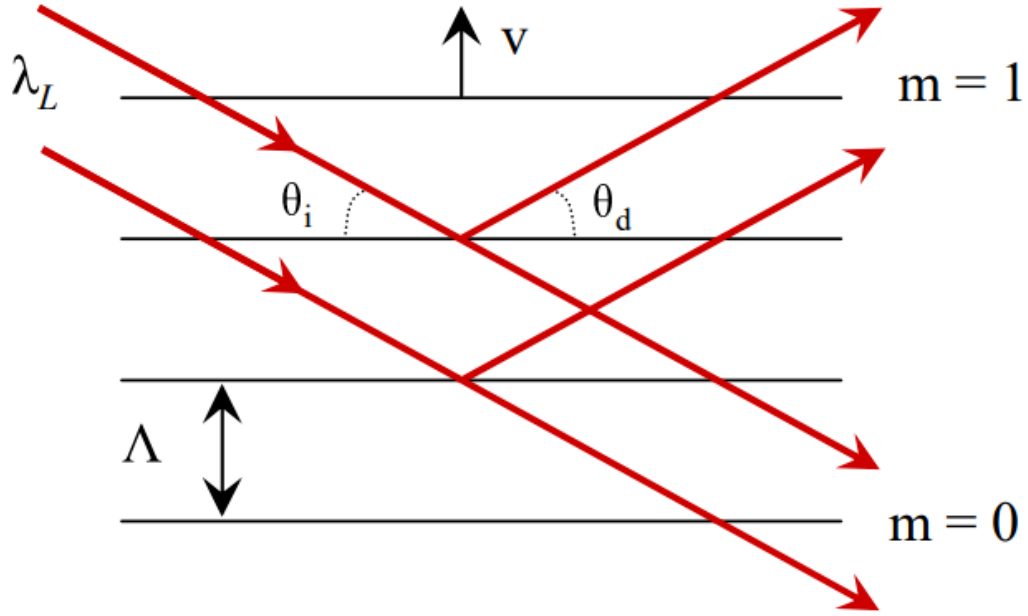

Figure 3.3: Illustration of the Bragg diffraction inside the AOM device [27].

In which n is an integer number, λ_L is the wavelength of the incoming laser beam, Λ is the acoustic wavelength (same frequency of the control RF signal) and θ_d is the angle between the scattered light in relation to the wavefront of the acoustic waves inside the AOM. Therefore, the Bragg's law applied to the case of the AOM is given below [27].

$$n\lambda_L = 2\Lambda sin(\theta_d) \tag{3.2}$$

Also, the change in frequency of the light after interacting with the acoustic waves (phonons) is given by the following relation.

$$\Delta f = m \cdot f_{RF} \tag{3.3}$$

In which m is the number of interacting phonons and f_{RF} is the frequency of the RF signal from an AWG. Additionally, the ratio of the intensity of the $1st$ order diffracted laser beam with

respect to the incident laser beam R is related to the intensity of the RF signal I_S through the following relation [28].

$$R \propto sin^2(\sqrt{I_S}) \tag{3.4}$$

In the end, the AOM will be used in order to act as an electronic chopper for the incoming laser beam by using the -1 order of the Bragg diffraction instead of using a mechanical chopper (which is suitable only to low frequencies).

3.2.2 Hollow Cathode Lamp

For the source of neutral Barium atoms, we use a Hollow Cathode Lamp (HCL) from *SpectroLamps (Model HC*004*)*, which consists of an enclosed environment filled with a noble gas, like argon, for instance, that prevents the formation of molecules. The working principle consists in applying a voltage between the anode and the cathode, with the second one being coated with a thin layer of Barium. This voltage ionizes the gas inside the lamp and it is accelerated towards the cathode and when the collision happens, neutral Barium atoms are detached from the cathode, creating a low density Ba gas inside the lamp [29]. In the following figure there is an illustration of the HCL.

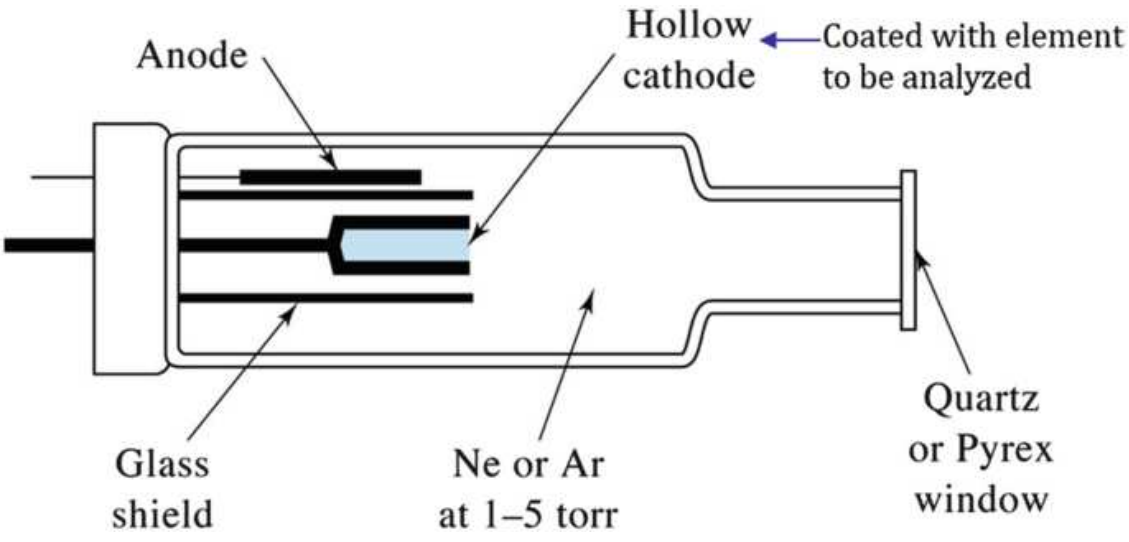

Figure 3.4: Illustration of a Hollow Cathode Lamp (HCL) working mechanism [30].

Additionally, in the HCL device, the voltage between the anode and the cathode is controlled directly by the set electrical current.

3.2.3 VECSEL LASER

We use in the present work a laser from the company Vexlum (Model VALO SHG - single frequency 553 nm), which is described as a Vertical-External-Cavity Surface-Emitting Lasers (VECSELs) type. This laser system is composed of a semiconductor device consisting of a quantum well, then the optical pumping happens by the use of an external laser diode. Additionally, in this system, the cavity is external and the dissipation of heat is made directly in the back of the semiconductor chip [31]. In the next figure there is an illustration of a VECSEL laser generation mechanism.

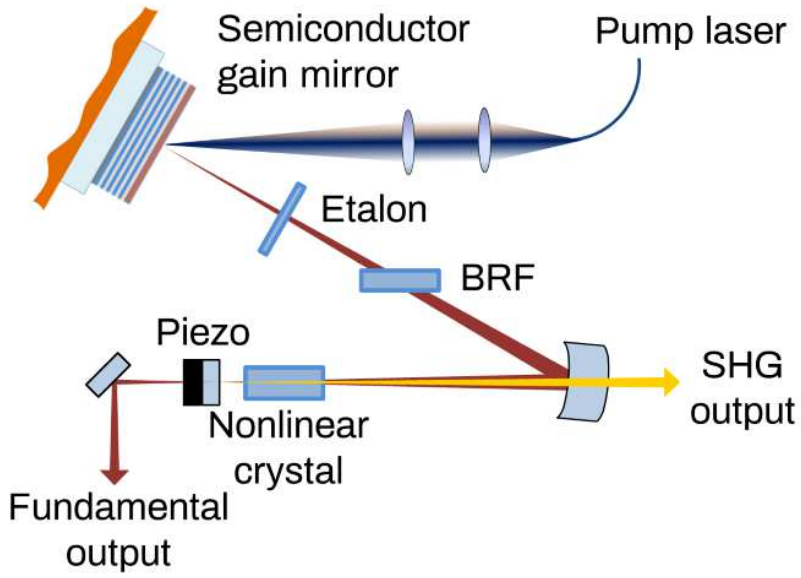

Figure 3.5: Illustration of a VECSEL laser's working mechanism [32].

In order to tune the frequency of the laser emission in this kind of laser, it is recommended to vary the temperature of the Etalon, of the Second Harmonic Generation (SHG) and of the Birefringent Filter (BRF), as well as rotating mechanically the BRF. For a fine-tuning of the laser frequency, a piezo driver can be connected to the laser, by generating a triangular wave from a signal generator to the piezo driver.

The Etalon acts as a filter that chooses a short wavelength variation, the BRF is a crystal that selects the desired wavelength given its rotation position and temperature and the SHG is a nonlinear crystal that also has the property of changing the wavelength of the laser light through its temperature [33].

3.3 Doppler spectroscopy

As a first step for the experimental setup development of the polarization spectroscopy, a Doppler spectroscopy is performed in order to determine the Doppler absorption when the laser light interacts with the Ba atoms in the HCL. Also, this technique of Doppler spectroscopy is also suitable to determine how the VECSEL laser behaves and the usage of the piezo driver (*THORLABS: Model MDT693B*) which amplifies a signal from a waveform generator with a gain of 15 times, which is used for the laser frequency stabilization of the 553.7 nm transition.

Firstly, in the figure below there is a schematics of the experimental apparatus of the Doppler spectroscopy technique.

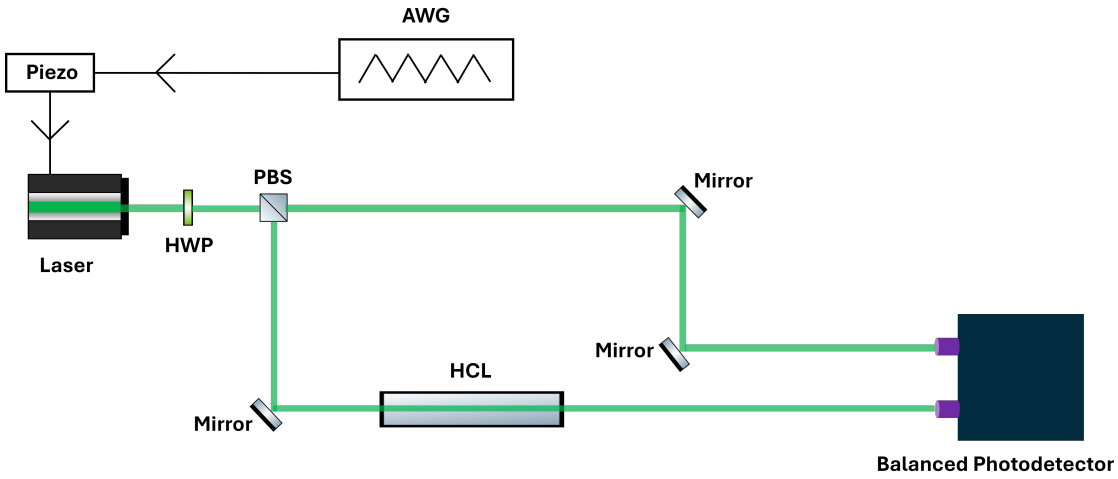

Figure 3.6: Illustration of the Doppler spectroscopy setup, which was designed by using the ComponentLibrary drawings [24]. ComponentLibrary by Alexander Franzen is licensed under a Creative Commons Attribution-NonCommercial 3.0 Unported License.

In this configuration, the laser beam is split into two paths after the Polarizing Beam Splitter (PBS) and their power is regulated through the Half-Wave Plate (HWP). Then, the transmitted laser beam after the PBS is reflected by mirrors and then it goes directly to one of the balanced photodetector inputs. Additionally, the reflected light after the PBS is reflected by a mirror, as shown in the figure above, and then it passes through the HCL and then it reaches the other input of the detector. It is important to emphasize that we use a balanced photodetector (differential photodiode) to measure and subtract light intensity variations.

For determining the Doppler absorption, an experiment was realized with a systematic procedure. Firstly, the Etalon, SHG and BRF temperatures, as well as the BRF rotation of the

VECSEL laser were adjusted in order to achieve the frequency of 541.4330 THz (transition frequency equivalent to the wavelength of 553.701 nm in the Ba atom) [34]. The measurement of the laser frequency was made by sending part of the light right after the laser output to an optical fiber connected to a collimator with an efficiency of around 5 % to a Wavemeter (*HighFinesse: Model WS*8 − 2).

With the use of a wave signal generator (*Tektronix: Model AFG*1022), a triangular wave signal with 6 Hz and with a minimum and maximum voltage of 1.5 V and 5.5 V, respectively, was applied in the piezo driver of the VECSEL laser and the same signal was inserted in one channel of a digital oscilloscope (*Tektronix: Model TBS*1000*C SERIES*). Firstly, with the HCL off, the HWP was rotated until the same intensity of both laser beams were equal to 1 mW each, which were measured with an Optical Power Meter (*THORLABS: Model PM*400), meaning that the difference of the signal of the two inputs of the photodetector (*THORLABS: Model PDB*220*A*2/*M*) is equals to zero. This was measured in the oscilloscope. Secondly, the HCL was turned on by adjusting a current of 15 mA. An image of the experimental setup is presented below.

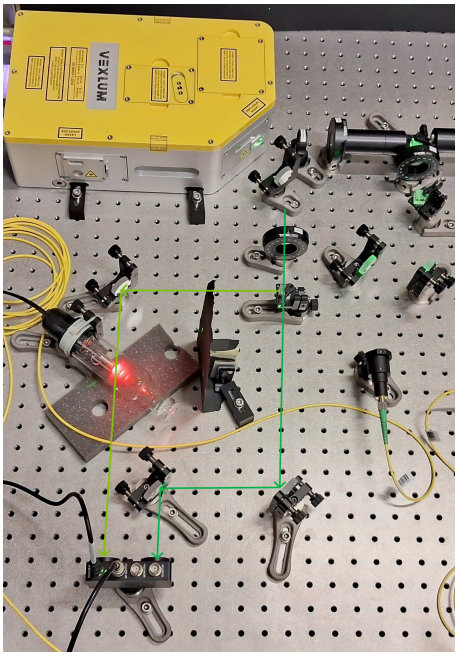

Figure 3.7: Experimental apparatus of the Doppler spectroscopy technique.

The green arrows represent the two paths of the laser beams, in which the optical components were positioned exactly as in the illustration from the Figure 3.6.

3.4 Experimental description of the polarization spectroscopy apparatus

In order to lock the VECSEL laser, the polarization spectroscopy technique must be performed in a functional way to have a Doppler-free signal. Consequently, the schematics represented in the Figure 3.1 was mounted in the optical table and during the experiments a few modifications were made in order to improve the quality of the polarization of the laser beams, which ends up improving the signal collected by the balanced photodetector. In the following image there is the schematics related to the polarization spectroscopy technique.

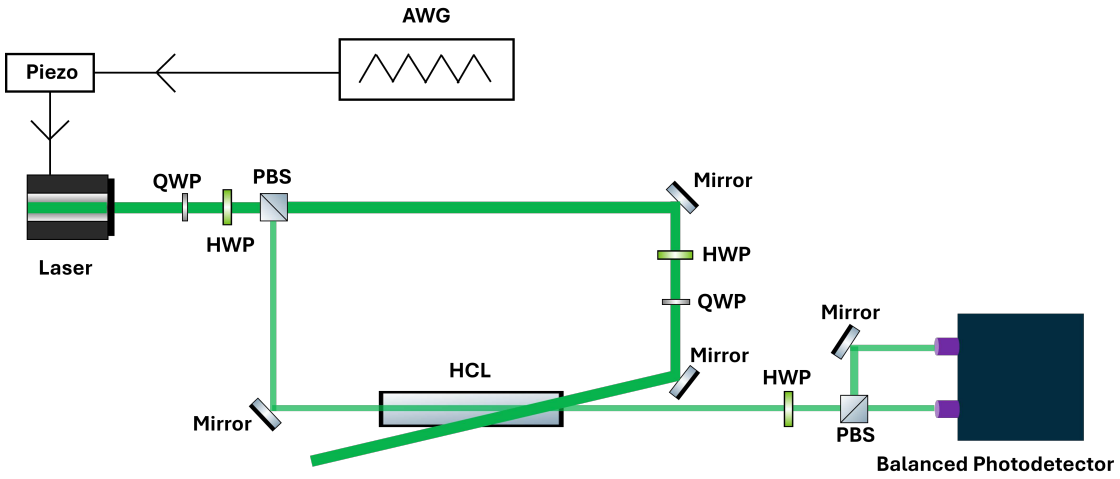

Figure 3.8: Illustration of the polarization spectroscopy setup, which was designed by using the ComponentLibrary drawings [24]. ComponentLibrary by Alexander Franzen is licensed under a Creative Commons Attribution-NonCommercial 3.0 Unported License.

In the schematics above there are two paths, the one associated to the thicker beam is the pump one and the other path (thinner beam) is the probe one. Both the paths will be explained below in this respective order.

The experiment starts with the incoming laser light that crosses a QWP and a HWP, which act in conjunction to control the polarization and intensity of the light. What is done firstly is to measure the transmitted light power with the Optical Power Meter, after the first PBS and adjust it accordingly the QWP and the HWP in order to set the power to zero (4.5 μW in our case). Then, without touching the QWP anymore, the HWP was rotated until a few mW were achieved in the transmitted beam and hundreds of μW in the reflected beam. With this procedure, we guarantee that after the PBS, the transmitted light (pump beam) is as best

horizontally polarized as it can and the same for the vertically polarized reflected light (probe beam).

Regarding the pump beam, it is reflected by a mirror and then it goes first to a HWP that regulates the power and rotates the polarization of the beam, then it passes by a QWP in order to have right circularly polarized (σ_+) light, by adjusting its position through rotation. Consequently, this strongly powered right circularly polarized light beam is reflected again by a mirror and then it interacts with the neutral Ba atoms in the HCL to saturate the P level with $m = +1$.

On the other hand, the probe beam goes in another path after the PBS, in which it is reflected by a mirror, then it interacts with the Ba atoms in the HCL. After this, it goes to a HWP in which it has its vertically linear polarization rotated and then it splits into a PBS again, in which now the transmitted light goes into one of the channels of the balanced photodetector and the reflected one is then reflected again by a mirror and, then, it goes to the other channel. In this way, one channel receives the projected component of the intensity of the probe beam in the x axis and the other channel receives the projection in the y axis. Additionally, the probe and pump beams were aligned by adjusting the positions of the mirrors with the goal of aligning the pump and probe beams to be as counter-propagating as possible, considering the experimental limitations. An image of the experimental setup is presented below.

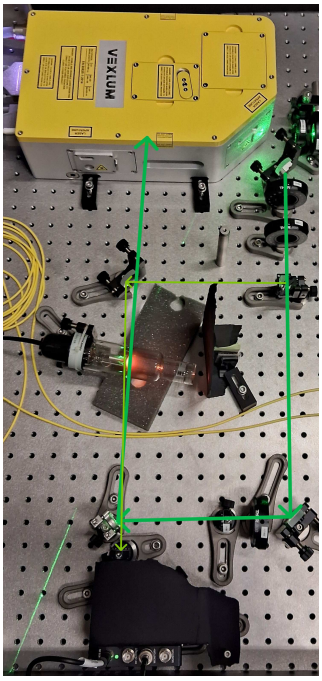

Figure 3.9: Experimental apparatus of the polarization spectroscopy technique.

Again, the experimental apparatus was designed exactly as the illustration of the Figure 3.8 and the cover in the picture is to avoid environmental light to come into the photodetector, in order to improve the quality of the signal. An image of this last part without the cover is shown in the figure below.

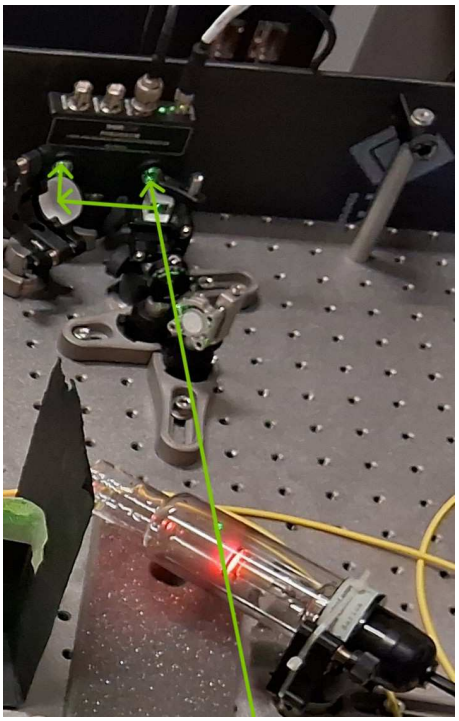

Figure 3.10: Zoom of the experimental apparatus of the polarization spectroscopy technique in the final part with only the probe beam and without any cover.

With the use of the wave signal generator, a triangular wave signal with 6 Hz and with a minimum and maximum voltage of 1.945 V and 3.955 V, respectively, was applied in the piezo driver of the VECSEL laser and the same signal was inserted in one channel of the digital oscilloscope. Firstly, with the HCL off, the HWP close to the photodetector was rotated until the same intensity of both components of the probe beam were equal and this procedure was done by inserting the signal in the other channel of the oscilloscope. Secondly, the HCL was turned on by adjusting a current of 15 mA. The pump beam power measured by the Optical Power Meter is 3.559 mW and the probe beam has a power of 0.484 mW and they were obtained after optimizing the signal quality and minimization of the width of the Doppler-free signal with the oscilloscope.

For the determination of the intensities of the laser beams, it is important to know the area of the beam and this is done with the use of a blade mounted in a support, in which the light

is blocked by the blade, then with a rotating axis the blade is moved by the distance of 0.1 mm and, then, the transmitted light is recorded with the use of the Optical Power Meter for each of the blade's position in this transit-type method. In our case, as the shape of the beam is practically circular, it was necessary only to measure the vertical variation of the blade's position and the transmitted power. This is shown in the figure below, along with a fitting with the error function.

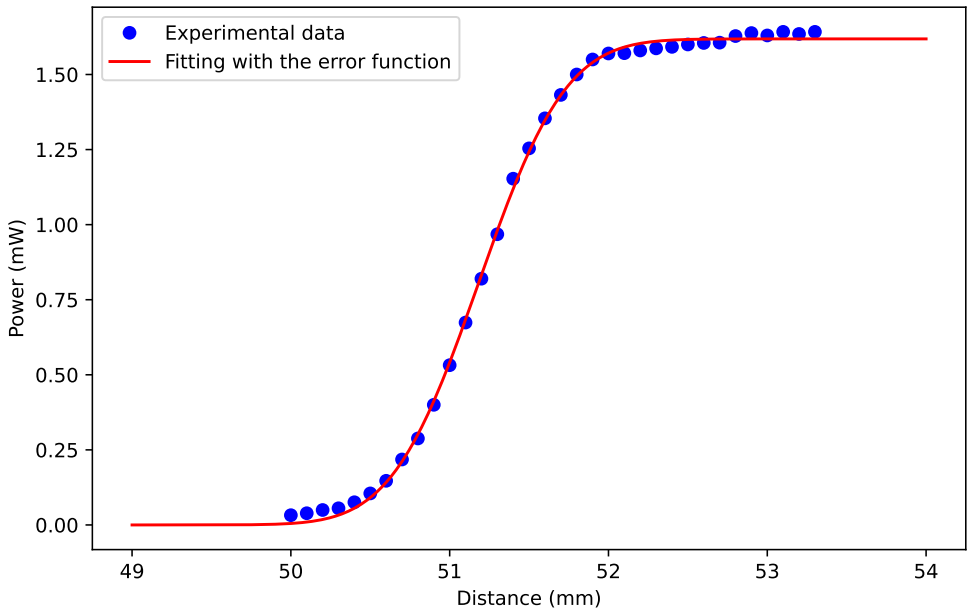

Figure 3.11: Graph of the variation of the power transmitted through the transit method in function of the position of the blade. Also, it is present the fitting curve with the error function, in order to estimate the diameter of the beam.

The error function used in this fitting is given by the expression below [35, 36].

$$f(x) = \frac{L}{2}\left[1 + \text{erf}[k(x - x_0)]\right] \tag{3.5}$$

In which $L/2$ is the half of the variation in power, x_0 is the associated midpoint in the position range, x is the position coordinate of the blade and k is the steepness of the curve. Therefore, considering the diameter of the beam associated to the variation of the power of the transmitted laser beam from 0.5% to 99.5%, the expression that calculates the diameter is given below [35, 36].

$$D = \frac{2 \cdot erf^{-1}(0.99)}{k} \tag{3.6}$$

The diameter from the fitting with the error function is $D = (2.22 \pm 0.04)$ mm and the associated area is $A = (3.872 \pm 0.001)$ mm^2. Additionally, the fitting coefficient is adequate since it is $R = 0.9992$. Also, the theoretical value of the saturation intensity, given a decay rate of $\Gamma = 2\pi \cdot 18.9$ MHz and a wavelength of $\lambda = 553.701$ nm is given by the following relation [37].

$$I_{sat} = \frac{\hbar\omega^3\Gamma}{12\pi c^2} \tag{3.7}$$

In which c is the speed of light in vacuum and ω is the angular frequency of the atomic transition. Therefore, the theoretical calculation gives an intensity of $I_{sat} = 0.146\ mW/mm^2$. Additionally, given that the saturating pump beam has a power of 3.559 mW and the area of the beam was calculated through the fitting of the S-shaped curve with the transit method, by doing the simple ratio of these quantities, respectively, we obtain the intensity of the pump beam, which is $I_{pump} = (9.19 \pm 0.05) \times 10^{-1}\ mW/mm^2$.

As the intensity of the pump beam is larger than the saturation intensity, then, indeed, the saturation of the population certainly occurs. Additionally, the intensity of the probe beam, calculated with the same method is $I_{probe} = (1.250 \pm 0.006) \times 10^{-1}\ mW/mm^2$, which is both smaller than the saturation intensity and high enough to result in a good signal in the photodetector.

Another consideration that must be taken is that one sided glass window of the HCL also absorbs part of the laser beam intensity and a method to quantify it consists in measuring the laser beam before and after crossing the HCL (when it is turned off) and the square root of the ratio between the output and input powers gives the transmission coefficient [12].

In our case, this transmission coefficient is $\sqrt{0.085} \approx 0.3$, meaning that 70% of the beam's intensity is absorbed by one glass window of the HCL. So, the actual intensities of the pump and probe beams are $I_{pump} \approx 2.8 \times 10^{-1}\ mW/mm^2$ and $I_{probe} \approx 3.8 \times 10^{-2}\ mW/mm^2$, in which both still satisfy the relative conditions with respect to the saturation intensity. Furthermore, we put two lenses in order to double the beam size to try to improve the signal even further, but it did not change the quality of the signal at all, then these lenses were removed. In the next figure there is a comparison of the HCL before and after use in the experiment and we can see visually the darkening of the glass window of the lamp through the usage of the device in the experiments.

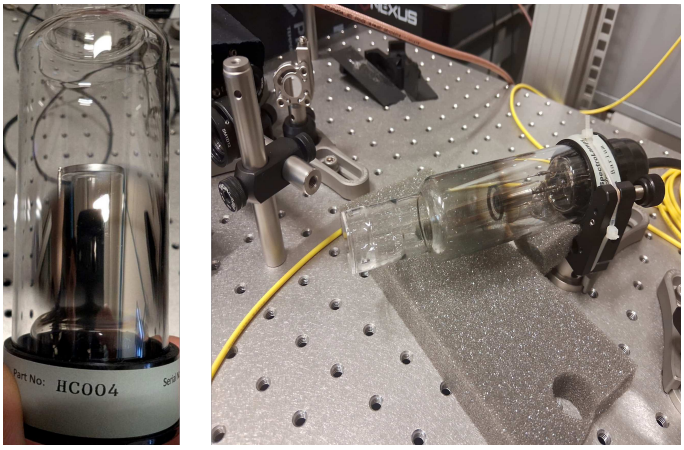

Figure 3.12: On the left there is an image of the HCL before using it and on the right, it is a picture of the HCL after using it.

3.5 Laser lock-in with polarization spectroscopy

From the polarization spectroscopy experiment, we used the same powers of the pump and probe beams, as well as the same configuration of the optical components, but to lock the laser frequency, two additional parts are added to the optical table, the AOM and the RedPitaya platform, respectively.

Firstly, the updated and final schematics of the experiment is shown in the figure below containing all the optical and electronics elements.

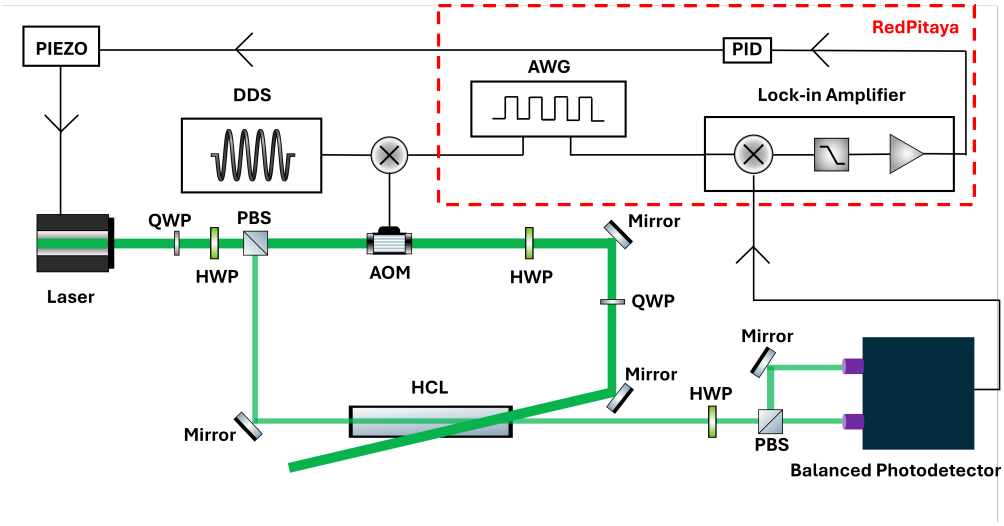

Figure 3.13: Illustration of the final experimental setup to lock the laser frequency, which was designed by using the ComponentLibrary drawings [24]. ComponentLibrary by Alexander Franzen is licensed under a Creative Commons Attribution-NonCommercial 3.0 Unported License.

Additionally, the image of the final experimental apparatus used to lock the laser frequency is shown in the figure below and it will be detailed in the next paragraphs.

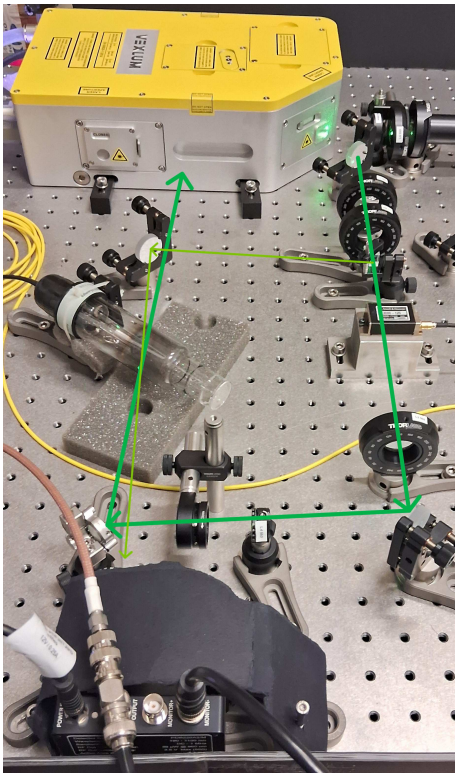

Figure 3.14: Experimental apparatus of the final setup for the lock-in of the laser frequency.

Firstly, the AOM was inserted and aligned in the path of the pump beam in the function of a chopper. The AOM was supplied with a RF signal of 80 MHz by the RF signal generator, then, the -1 order was chosen to be sent to the HCL as the pump beam (the other orders were blocked with an iris). But, between the RF generator and the AOM, there is a laboratory made amplifier that has a gain of 45 dBm, measured with a Spectrum Analyser (*TinySA: Model ULTRA*). Then, by measuring with the Optical Power Meter the power of the -1 order beam after the AOM and the incident beam before the AOM and taking the ratio (AOM efficiency), we optimized the value of the power of the RF generator in -16.5 dBm (associated to the maximum AOM efficiency obtained), which results in 28.5 dBm (708 mW) after the amplifier [38] and the efficiency is $R = 72\%$.

After that, we changed the position of the HWP after the AOM to optimize space and the RedPitaya was connected according to the Figure 3.13 above. In order to perform the laser lock-in, we used a software based in Python language called Linien, that does the function of

lock-in via PID control [39]. Then, in the Linien software, the AOM's modulation frequency was chosen (after optimization) as 32 kHz, with a modulation amplitude of 1 Vpp and a sweep speed of 7.5 Hz. The RedPitaya sends an output square wavesignal with this frequency modulation to the input of the RF generator, which is connected through the laboratory amplifier to the AOM.

Then, the second output of the RedPitaya is connected to the piezo driver, that is connected to the VECSEL laser. Then, the signal from the difference of the two channels of the balanced photodetector is split into two through coaxial cables and they are connected to the two inputs of the RedPitaya, in which one input channel only reads the signal and the other one takes the signal to perform both a derivative and demodulation in order to have an error signal to lock the laser through the PID control.

4

Data analysis and results

4.1 Results of Doppler spectroscopy

In the figure below there are two signals obtained from the oscilloscope when the HCL is off. The first one is the yellow signal, representing the difference of intensities of the two input channels of the balanced photodetector, and, the second one is the triangular wave from the wave signal generator (in blue).

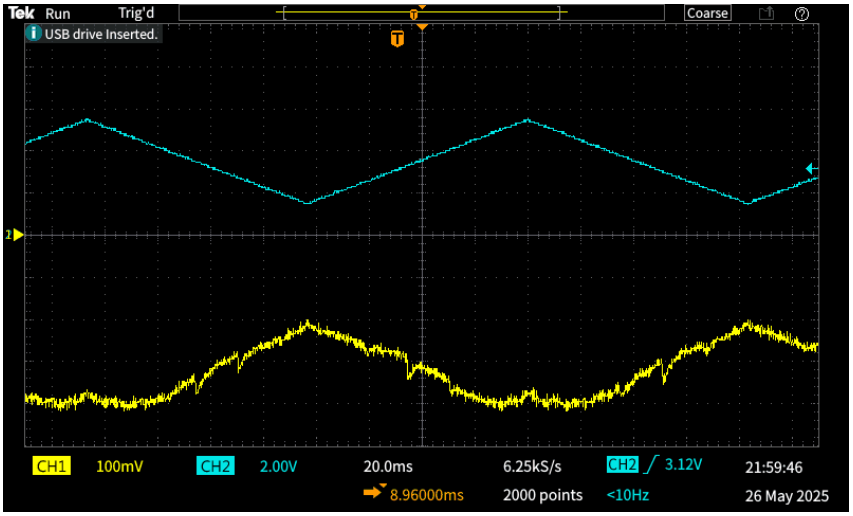

Figure 4.1: Photodetector signal (yellow) and triangular wave from the signal generator (blue), obtained with the oscilloscope in the Doppler spectroscopy experiment when the HCL is off.

After turning on the HCL, we obtain the Doppler absorption signal of the transition $6s^2\,{}^1S_0 \rightarrow 6s6p\,{}^1P_1$ as shown in the next figure from the oscilloscope.

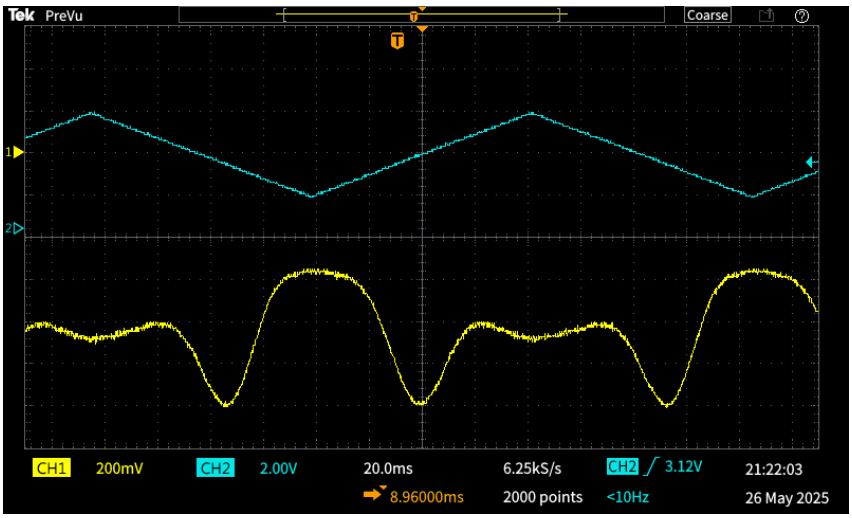

Figure 4.2: Photodetector signal (yellow) and triangular wave from the signal generator (blue), obtained with the oscilloscope in the Doppler spectroscopy experiment when the HCL is on.

From the Wavemeter readout, the piezo driver scanned 2.6 GHz with its center frequency (where the center of the Doppler broadening was positioned) in 541.4332 THz, in which the expected value for this atomic transition is in 541.4330 THz [34]. In order to perform a quantitative analysis of the Doppler absorption from the oscilloscope data, a Python code was developed to do the following: normalize the two signals from 0 to 1 scale, apply 1 minus the yellow signal to have the absorption instead of the transmission of the laser beam and, finally, apply a transformation to convert the time in frequency, with the following expression.

$$f = t \cdot \frac{S_R}{T_{1/2}} \tag{4.1}$$

In which f is the frequency, t is the time to be converted in frequency scale, $S_R = 2.6$ GHz is the scan range and $T_{1/2} = 82.8$ ms is half of the period of the triangular wave signal. Then, the Python code fits a Gaussian curve with a linear background in order to obtain the Full Width at Half Maximum (FWHM) and the fitting coefficient R^2. The analysis of this data in Python is presented in the following figure.

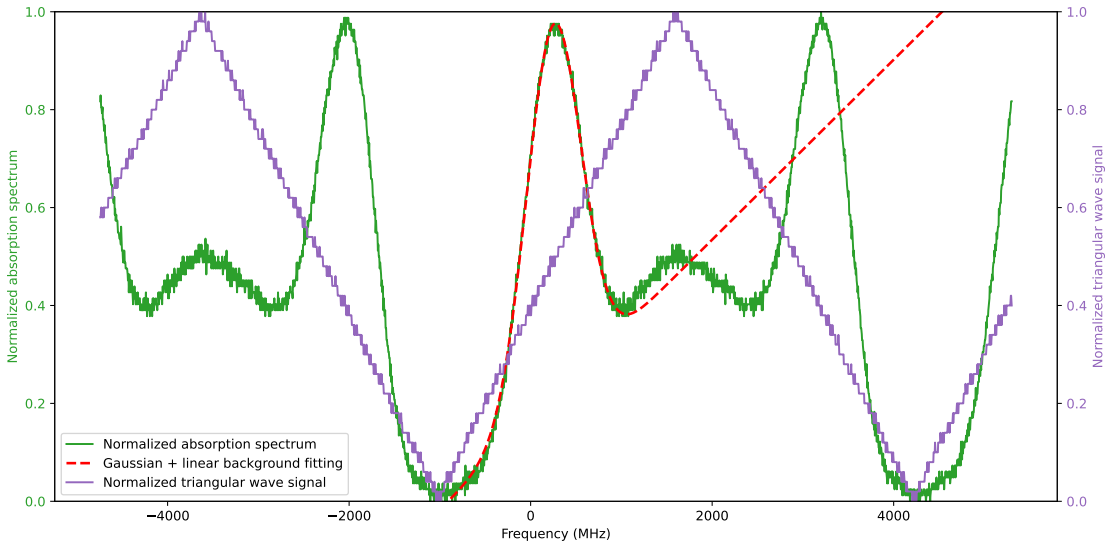

Figure 4.3: Photodetector signal converted to normalized absorption of light in function of the frequency with an arbitrary reference point (green), normalized triangular wave signal which is the input of the piezo driver (purple) and Gaussian fitting with a linear background (red).

The model for the fitting of the signal of the figure above is given by the relation below.

$$f(x) = A \cdot \exp\left(-\frac{(x-\mu)^2}{2\sigma^2}\right) + mx + c \tag{4.2}$$

In which A is the amplitude of the curve, μ is the mean value, σ is the variance of the Gaussian, m is the slope of the linear background and c is the intercept of the linear background. From the fitting, the FWHM obtained is (707 ± 3) MHz and the quality of the fitting is good since $R^2 = 0.99808$. Also, as the signal of the Doppler broadening has a high quality, for the fitting procedure it was not needed to subtract the background signal when the HCL is off.

And for a comparison with the theoretical value for the FWHM, we can use the relation below [18].

$$\text{FWHM} = 2\sqrt{2\ln 2} \cdot \frac{1}{\lambda}\sqrt{\frac{k_b T}{m}} \tag{4.3}$$

And by considering $T = 500$ K, the theoretical Full Width at Half Maximum is FWHM = 740 MHz, meaning that the experimental result is reliable and compatible with the order of magnitude of the theoretical prediction. Additionally, by using the Expression 4.3 above, the temperature of the Ba gas of atoms considering the FWHM obtained through the fitting

procedure in the Doppler spectroscopy experiment is given below.

$$T_{exp} = (456 \pm 4)\, K \tag{4.4}$$

4.2 Results of polarization spectroscopy

In the figure below there are two signals obtained from the oscilloscope when the HCL is off. The first one is the yellow signal, representing the difference of intensities of the two input channels of the balanced photodetector, and, the second one is the triangular wave from the wave signal generator (in blue).

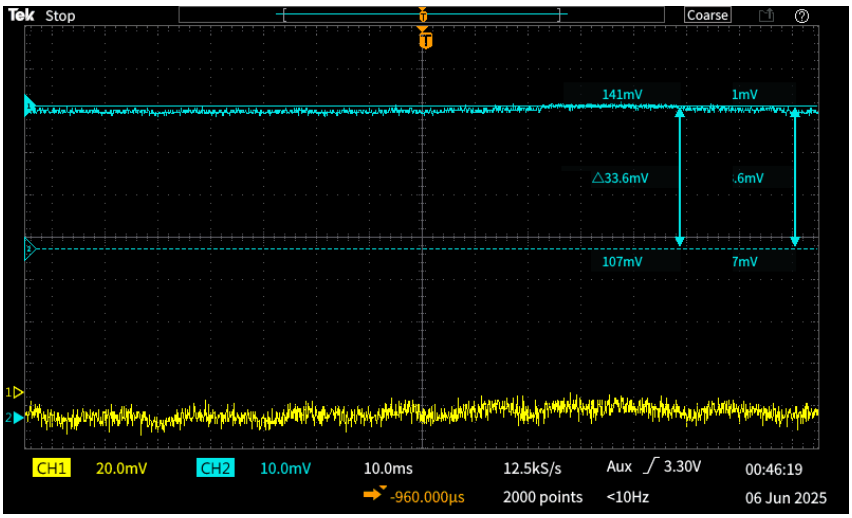

Figure 4.4: Photodetector signal (yellow) and triangular wave from the signal generator (blue), obtained with the oscilloscope in the polarization spectroscopy experiment when the HCL is off.

After turning on the HCL, we block the pump beam to visualize the signal and set this as the background for subtraction of the signal with the pump unblocked. This signal without a pump beam is shown in the next figure from the oscilloscope.

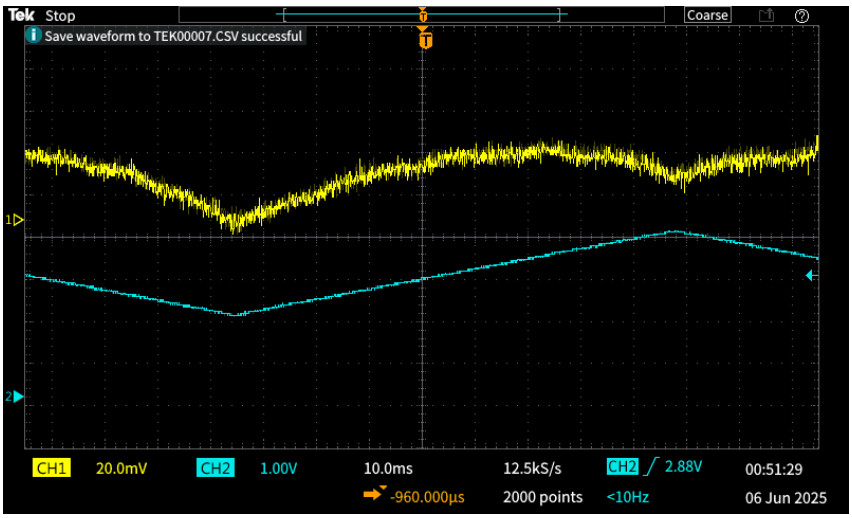

Figure 4.5: Photodetector signal (yellow) and triangular wave from the signal generator (blue), obtained with the oscilloscope in the polarization spectroscopy experiment when the HCL is on but the pump beam is blocked.

With the HCL on and with the pump beam also unblocked, we obtain a Doppler-free signal related to the transition $6s^2\,{}^1S_0 \rightarrow 6s6p\,{}^1P_1$ as shown in the next figure from the oscilloscope.

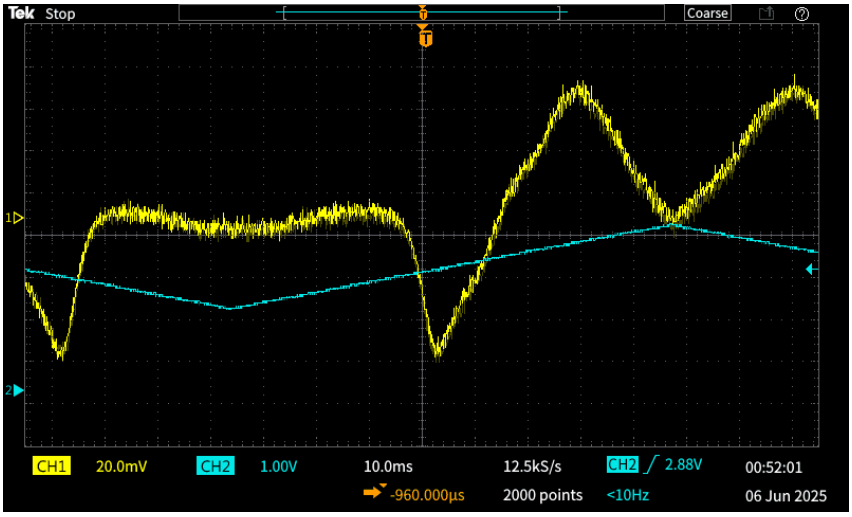

Figure 4.6: Photodetector signal (yellow) and triangular wave from the signal generator (blue), obtained with the oscilloscope in the polarization spectroscopy experiment when the HCL is on and the pump beam is unblocked.

From the Wavemeter readout, the piezo driver scanned 1.1 GHz with its center frequency (where the center of the Doppler-free signal was positioned) in 541.4330 THz, which is the expected value for this atomic transition. In order to perform a quantitative analysis of the Doppler-free signal from the oscilloscope data, a Python code was developed to do the following: subtract the yellow signal (difference of the two signals from the balanced photodetector)

when the pump beam is unblocked from the same signal when the pump beam is blocked (background signal), apply 1 minus the resulting signal to have the absorption instead of the transmission of the laser beam and, finally, apply a transformation to convert the time in frequency, with the Expression 4.1.

In which $S_R = 1.1\,\text{GHz}$ and $T_{1/2} = 82.8\,\text{ms}$. Then, the Python code fits a Lorentzian curve with a linear background, in order to obtain the Full Width at Half Maximum (FWHM) and the fitting coefficient R^2. The analysis of this data in Python is presented in the following figure.

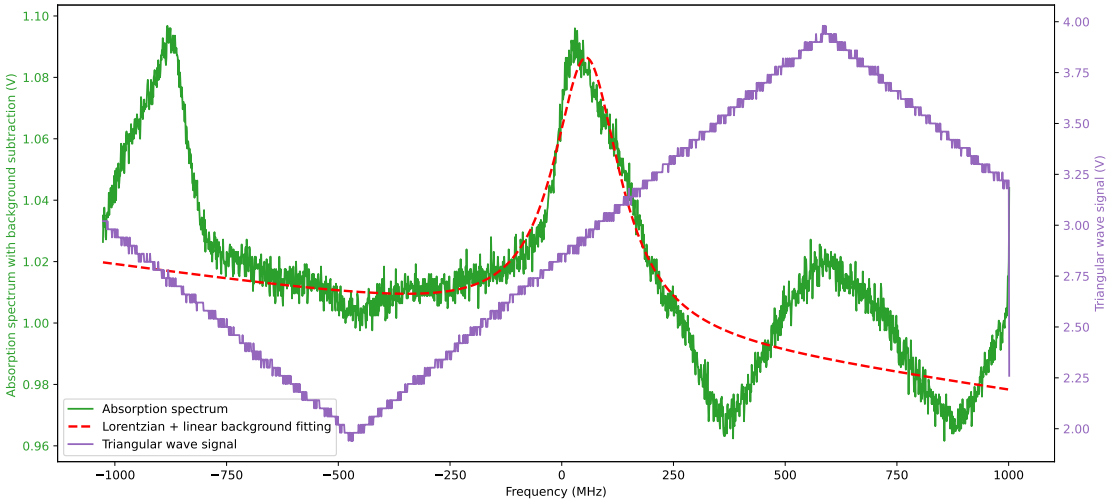

Figure 4.7: Photodetector signal when the pump beam is unblocked, subtracted by the background signal when the pump beam is blocked, then converted to absorption of light in function of the frequency with an arbitrary reference point (green), triangular wave signal which is the input of the piezo driver (purple) and Lorentzian fitting with a linear background (red).

The model for the fitting of the signal of the figure above is given by the relation below.

$$f(x) = A \cdot \left(\frac{\gamma^2}{(x-\mu)^2 + \gamma^2} \right) + mx + c \tag{4.5}$$

In which A is the amplitude of the curve, μ is the mean value, γ is the Half Width at Half Maximum (HWHM), m is the slope of the linear background and c is the intercept of the linear background. From the fitting, the FWHM obtained is (182 ± 4) MHz and the quality of the fitting is reasonable since the fitting coefficient obtained is $R^2 = 0.95016$. Therefore, since the decay rate of this transition is $\Gamma = 2\pi \cdot 18.9\,\text{MHz}$, consequently, the FWHM is around 10 times the natural linewidth of the atomic transition.

Now, keeping the HCL on and with the pump beam blocked, instead of getting the difference of the two input channels of the photodetector, only one channel was read through the oscilloscope and its signal is presented in the following figure.

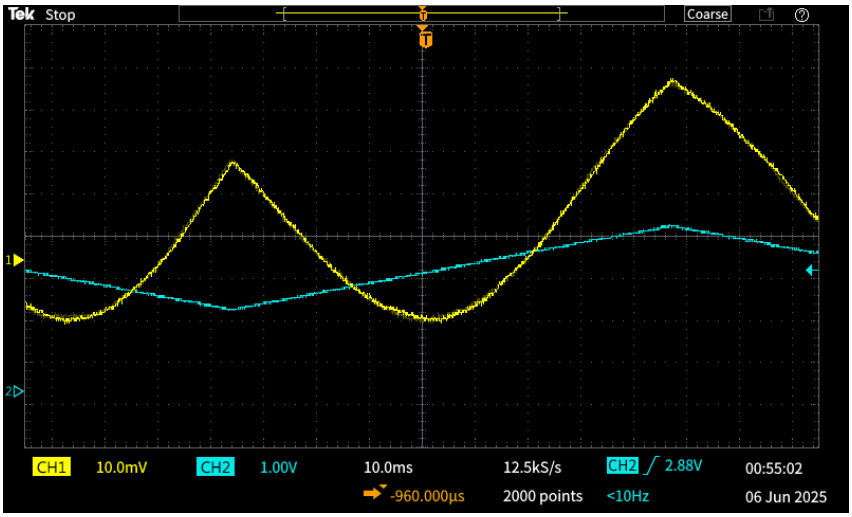

Figure 4.8: Photodetector's single channel signal (yellow) and triangular wave from the signal generator (blue), obtained with the oscilloscope in the polarization spectroscopy experiment when the HCL is on but the pump beam is blocked.

After that, unblocking the pump beam allowed us to visualize the Doppler broadening and, also, the Lamb peak. We see a Lamb peak because the signal of the oscilloscope is the transmission of the light, but in absorption visualization it is the Lamb dip, as already discussed in the previous sections. We see in the next figure this behavior of the signal.

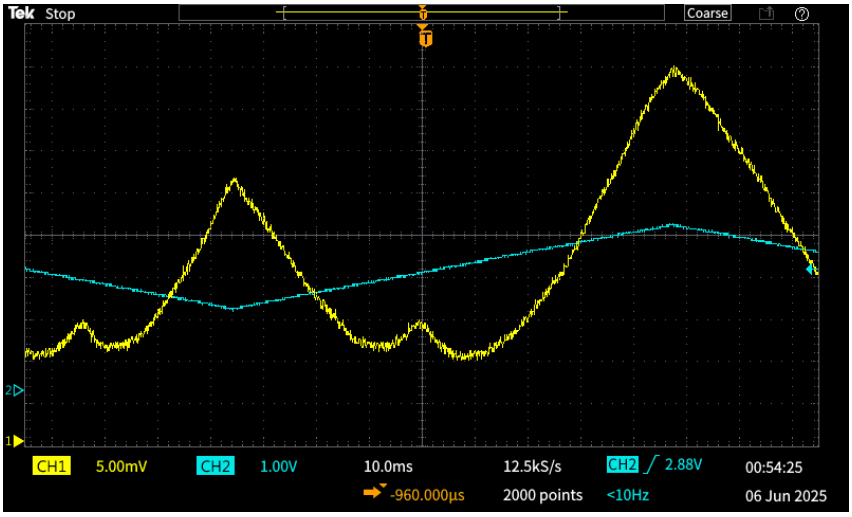

Figure 4.9: Photodetector's single channel signal (yellow) and triangular wave from the signal generator (blue), obtained with the oscilloscope in the polarization spectroscopy experiment when the HCL is on but the pump beam is unblocked.

As a result, the polarization spectroscopy experiment was able to take advantage of the polarizations of the pump and probe beams in order to have a Doppler-free signal, which is suitable to perform the lock-in of the laser. Additionally, for a matter of visualization, in the next figure both the signals of the difference of the two input channels of the photodetector and the single channel reading are recorded with the oscilloscope. This visualization allows us to see both curves superposed.

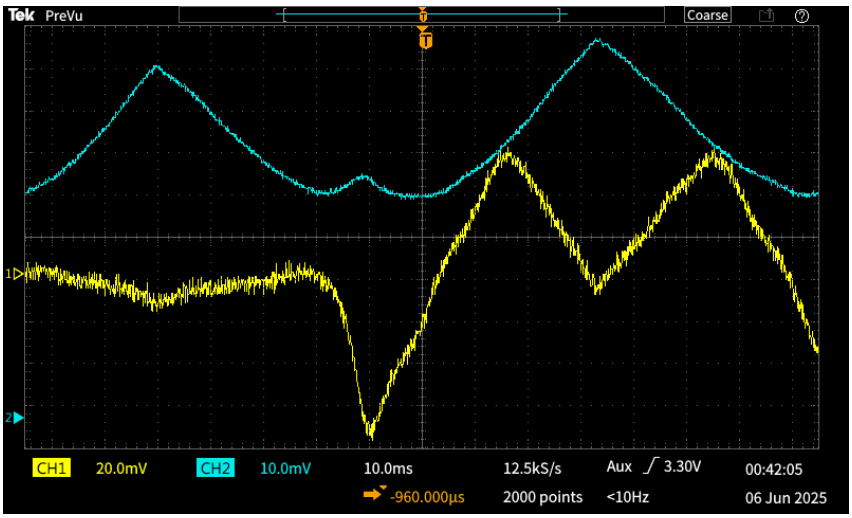

Figure 4.10: Photodetector's single channel signal (blue) and difference of the two input signals (yellow), obtained with the oscilloscope in the polarization spectroscopy experiment when the HCL is on but the pump beam is unblocked.

4.3 Results of the Laser lock-in

The result of the error signal performed by the RedPitaya (red) and the signal of the difference between the two channels of the balanced photodetector (blue) are shown in the next figure, considering a scan range of 700 MHz provided by a triangular wave signal generated by the RedPitaya with 1 Vpp directed to the piezo driver.

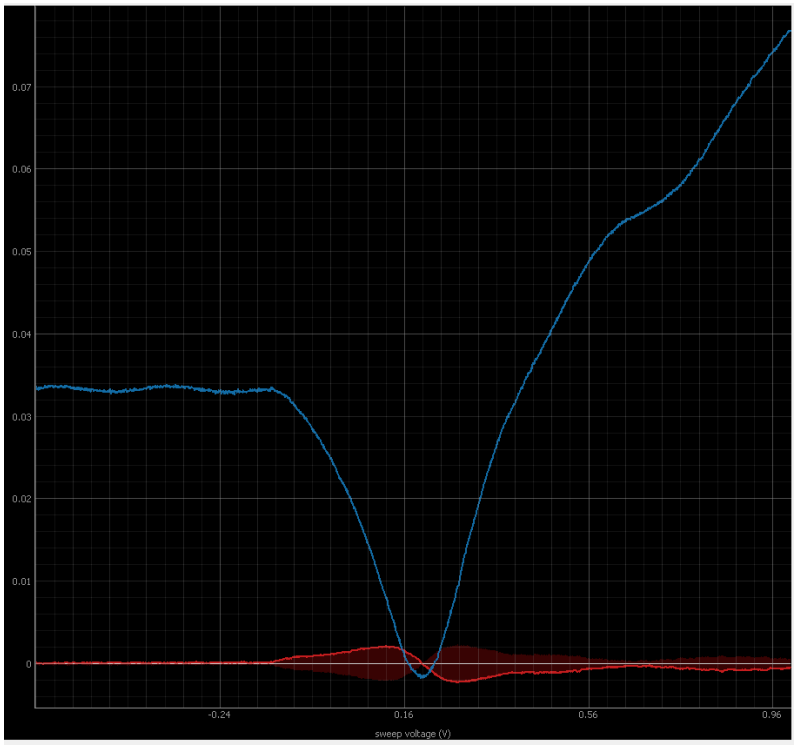

Figure 4.11: Difference of the two input signals from the photodetector (blue) and associated inverted error signal (red), obtained through the Linien software [39].

From the figure above we can see clearly the signal (blue) and its associated error (red). Then, the PID parameters were adjusted throughout a week, in order to optimize the quality of the lock-in and they were chosen in the Linien software as $P = 2000$, $I = 500$ and $D = 0$. In the next figure there is the evolution of the laser frequency through 11 hours of measurement in the Wavemeter, for both locked and unlocked laser.

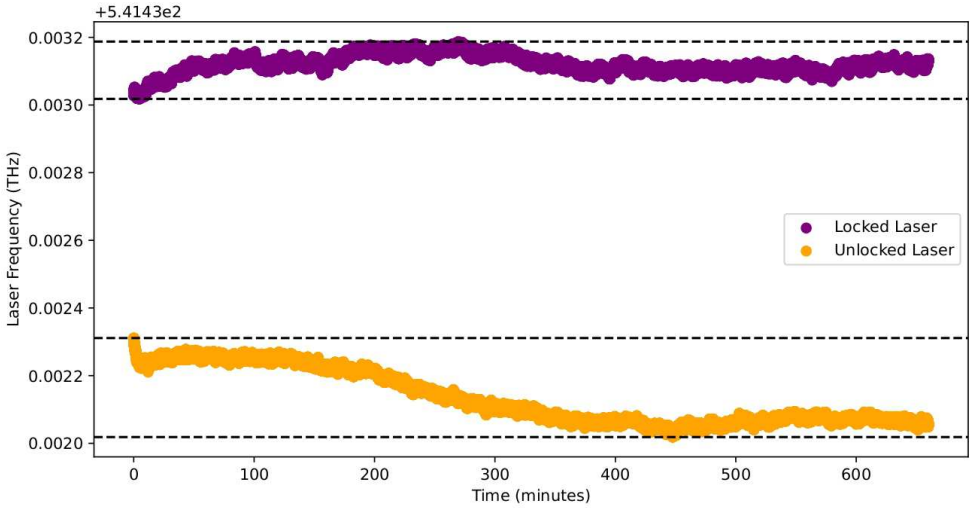

Figure 4.12: Locked and unlocked signals from the Wavemeter readout during 11 hours of long scan.

From the figure above, we notice that the locked laser matches the value of the reference frequency of the atomic transition, since the signal is between 541.4330 THz and 541.4331 THz, as expected. Also, the dashed black lines are present in the figure in order to visualize the drift in the long scan signal and we can notably see that the unlocked laser drifted much more in comparison with the locked case. In this case, the locked laser has a shorter standard deviation (27 MHz) when compared to the unlocked one (80 MHz). This means that the unlocked laser drifted the laser frequency throughout the time, while the locked laser did not drift the signal in the same way, meaning that the PID control effectively decreased the standard deviation of the laser frequency when compared to the unlocked laser by a factor of approximately 3 times.

Additionally, the Allan deviation analysis was performed in a Python code in order to verify the stability of the locked and unlocked laser for this long scan. This technique relies on the division in uniform intervals of time, then it takes the associated mean to check how it varies through the time during the long scan. In the next figure, it is presented a log-log scale graph with the Allan deviation analysis for both locked and unlocked laser.

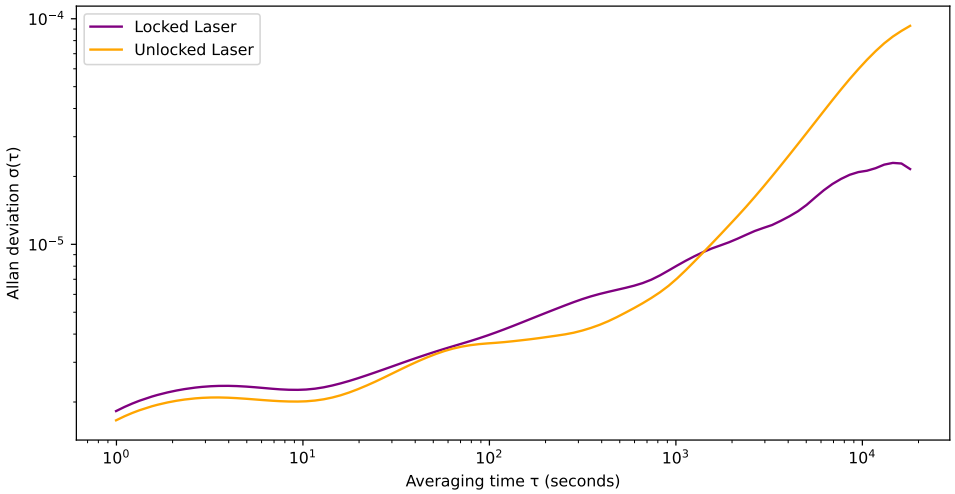

Figure 4.13: Allan deviation analysis of the locked and unlocked signals from the Wavemeter readout during 11 hours of long scan.

From the figure above, it is noticeable that the cumulative behavior of both scenarios are similar, which means that in short interval analysis of the frequency deviation for both locked and unlocked laser, during a long scan measurement, the signals behave in a similar way. Essentially, for a short time the laser noise is similar for both the locked and unlocked scenarios, however, for the range of hours, it is visible from the Allan deviation analysis that the locked laser drifts much less in comparison with the unlocked one, since we can visualize in the Figure 4.13 that after $\approx$ 25 minutes the unlocked laser drifts much more (higher values in the graph) and the two curves increase their separation through the time.

4.4 Results of the MOT simulation

By implementing numerically in Python the Equation 2.62, we were able to study the evolution of the population of each of the levels of the considered cooling cycle: $6s^2\,{}^1S_0$ (level 1), $6s6p\,{}^1P_1$ (level 2), $6s5d\,{}^1D_2$ (level 3), $6s5d\,{}^3D_2$ (level 4) and $6s5d\,{}^3D_1$ (level 5). In the following figure, there is a comparison between these populations evolution considering only the cooling transition without any repumping lasers and with 1, 2 and 3 repumpers, respectively, as indicated in the Figure 2.1 considering these 5 levels. Additionally, the detuning of the laser that induces the cooling transition was set to $\delta_{21} = -\Gamma_{21} \cdot 2.4$, chosen based on the reference [9] and all the others we set at resonance ($\delta = 0$).

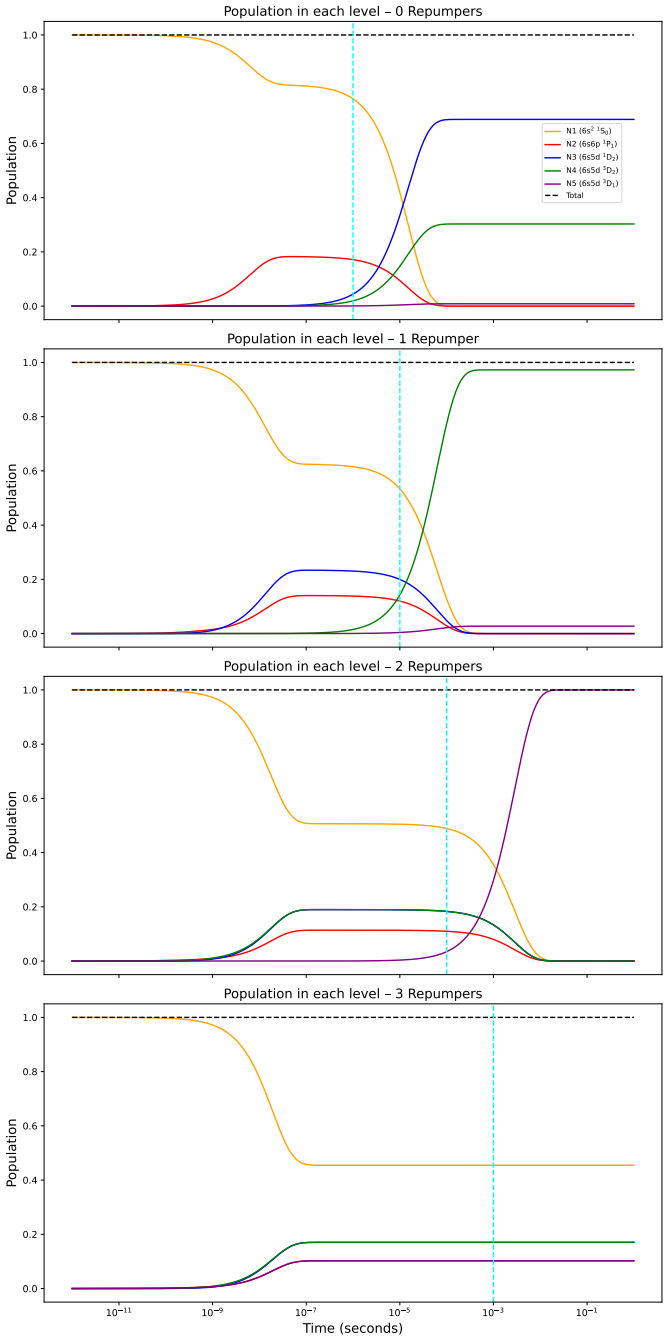

Figure 4.14: Comparison of the evolution of the population of the 5 energy levels in the Ba atom for $0, 1, 2$ and 3 repumping lasers. The parameters used in the simulation are the following: $T = 456\,K$, the laser powers are $P_{12} = 12\,mW$, $P_{32} = 5\,mW$, $P_{42} = 25\,mW$ and $P_{52} = 60\,mW$, with a beam radius of $1.5\,mm$. Additionally, the natural linewidth of the decays from the level 2 to the other ones are: $\Gamma_{21} = 1.19 \times 10^8\,rad/s$, $\Gamma_{23} = 0.0025 \times 10^8\,rad/s$, $\Gamma_{24} = 0.0011 \times 10^8\,rad/s$ and $\Gamma_{25} = 0.000031 \times 10^8\,rad/s$ [9]. The x axis is in log scale and the total simulation runs for 1 second.

From the figure above we can visualize the physics involved in the four cases as the population of each level evolves through the time. Also, we neglect the third term of the Expression 2.62 because we are considering in the simulation the absence of losses in the MOT, also the dynamics of the laser cooling happens too fast, then this approximation is still valid [21].

Firstly, with 0 repumpers, we observe a decrease of the ground state (level 1) and and increase of the excited state (level 2), as well as in a lesser scale a slight increase in all the metastable states, but because there are no repumping lasers, the populations that go to the excited state start decaying to the metastable states and get trapped there, also, their distribution varies with both their respective decay rates and degeneracies. In the end, all the population achieves a steady state in the three metastable states. Additionally, the dashed black line is the total population evolution, which is constant since there is conservation of the population, also, for each graph there is a dashed vertical line (cyan color) that marks the end of the effective cooling cycle, which is characterized by the time after which the population starts leaking out of the P state, so the atom stops scattering the cooling laser. Therefore, we can call it t_{end} and we chose them by analyzing when the level 2 (red color) of the figure above started decreasing again its population.

With respect to the simulation with 1 repumper, we observe again a decrease of the ground state (level 1) and and increase of the excited state (level 2) and the level 3, as well as in a lesser scale a slight increase in the other two metastable states. However, as now there is a repumper laser that brings back the population from the level 3 to the level 2, the level 3 also ends up with no population and the same happens with the levels 1 and 2. Also, the population is distributed in the steady-state regime in the levels 4 and 5. One important characteristic is that the cooling cycle takes longer to finish.

In the simulation with 2 repumpers, all the population ends up in the level 5 in the steady-state regime, since the second repumper also brings back the population from the level 4 to the level 2. Also, the levels 3 and 4 evolve in a similar trend because they have the same degeneracy and their respective natural linewidth have the same order of magnitude.

Finally, with all the 3 repumpers the cycle is completely closed, meaning that the steady-state of the populations of each level depends only on their degeneracies. This explains why the levels 2 and 5 ($J = 1$) have their populations with the same distribution. Similarly with the levels 3 and 4 ($J = 2$) and with the single level 1 ($J = 0$).

In order to estimate the optical force in function of the velocity of the Ba atoms in the center of a MOT ($x = 0$), we focus on the laser interaction with the energy levels in the cooling process. In a Python simulation, we consider two counter-propagating cooling laser beams for the cooling transition between the levels 1 and 2 and the other 3 repumpers are considered

to be perpendicular to the cooling ones (in this case the Doppler effect is not considered in the repumping cases). In order to calculate the population evolution of the 5 levels, again the Expression 2.62 was used, but with the difference now that there are two counter-propagating cooling lasers which contribute to the scattering rates and, also, that their detuning are Doppler shifted as $\delta_{12} \pm kv$.

Then, for each of the 4 scenarios we use the atomic populations calculated at the respective t_{end} in the Figure 4.14. Considering all these factors and given that the natural linewidth associated to the cooling transition is much larger than the other ones associated to the transitions to the metastable states, we can use the Equation 2.65 to simulate the MOT force in function of the velocity in the center of a MOT ($x = 0$). The result of the simulation considering all the configurations of the number of repumping lasers is shown in the next figure.

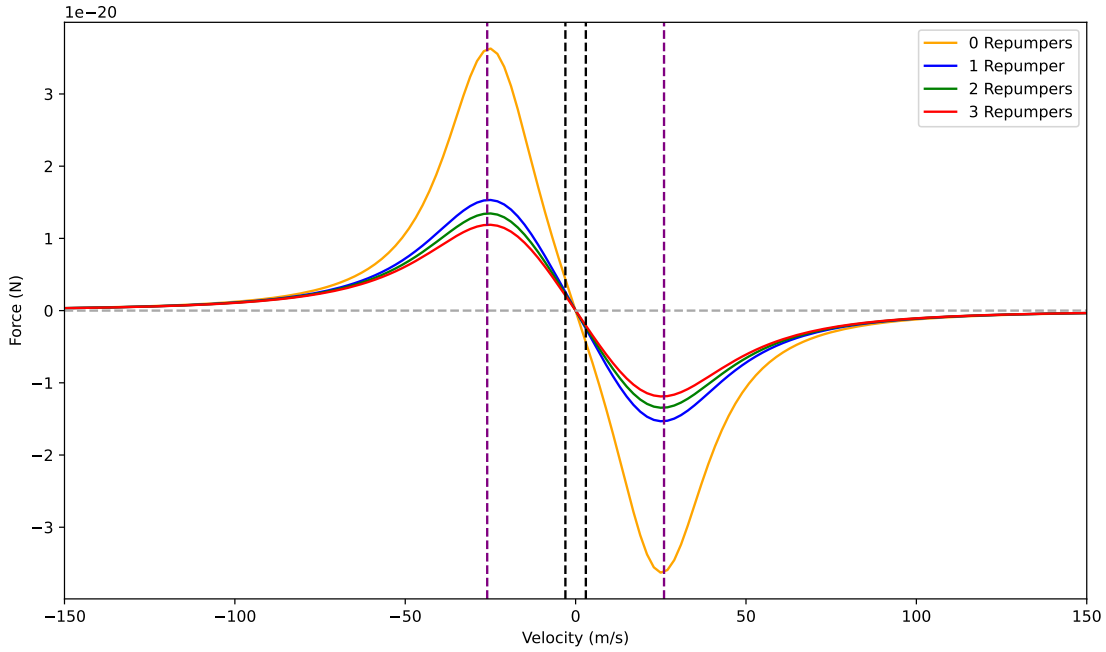

Figure 4.15: Force in function of the velocity of the Ba atoms in a MOT at $x = 0$ for 0, 1, 2 and 3 repumping lasers. The parameters used in the simulation are the following: $T = 456\,K$, the laser powers are $P_{12} = 12\,mW$, $P_{32} = 5\,mW$, $P_{42} = 25\,mW$ and $P_{52} = 60\,mW$, with a beam radius of $1.5\,mm$. Additionally, the natural linewidth of the decays from the level 2 to the other ones are: $\Gamma_{21} = 1.19 \times 10^8\,rad/s$, $\Gamma_{23} = 0.0025 \times 10^8\,rad/s$, $\Gamma_{24} = 0.0011 \times 10^8\,rad/s$ and $\Gamma_{25} = 0.000031 \times 10^8\,rad/s$ [9].

From the figure above, we notice that the linear region of the force in function of the velocity is approximately in the range from -26 m/s to $+26$ m/s (purple vertical dashed lines) and in order to perform a fitting of the linear region, a range of ± 3 m/s (black vertical dashed lines)

was chosen. Therefore, the results of the damping coefficients for 0, 1, 2 and 3 repumpers are given in the following table.

α_0 $(\times 10^{-21}\ kg/s)$	α_1 $(\times 10^{-21}\ kg/s)$	α_2 $(\times 10^{-21}\ kg/s)$	α_3 $(\times 10^{-21}\ kg/s)$
1.442 ± 0.002	0.8529 ± 0.0002	0.7651 ± 0.0004	0.6969 ± 0.0004

Table 4.1: Damping coefficients with 0, 1, 2 and 3 repumpers, respectively.

From this result we notice that the damping coefficient decreases when more repumpers are added and this is also seen in the figure above, since the amplitude of the force decreases as well for more repumpers.

In the end, given that the dynamics of the effective cooling cycle time is too short and that the MOT must capture an adequate range of velocities of Ba atoms, it is suitable to use all the 3 repumping lasers in order to close the cooling cycle.

5
Conclusions

After the realization of Doppler spectroscopy, it was possible to detect the Doppler broadening related to the transition $6s^2\,{}^1S_0 \rightarrow 6s6p\,{}^1P_1$. This signal has a FWHM of (707 ± 3) MHz. Additionally, the polarization spectroscopy technique allowed us to identify the Lamb dip in a Doppler background in the absorption spectrum of the probe beam. The technique of polarization spectroscopy resulted also in a Doppler-free signal with $FWHM = (182 \pm 4)$ MHz, that carries both the collisional effect broadening and the unavoidable natural linewidth.

This Doppler-free signal was utilized in order to lock the laser frequency with a PID control through the RedPitaya. Moreover, in 11 hours of long scan, the laser frequency with the lock-in activated has a standard deviation of 27 MHz, while the unlocked signal has an equivalent of 80 MHz and this shows the capacity of the locked signal to avoid drifts in the laser frequency for a long time.

Furthermore, the computational simulations of a MOT were performed and the evolution of the populations of the 5 considered energy levels of the Barium atom was obtained. These simulations considered 0, 1, 2 and 3 repumping lasers and the population behavior in the steady-state of the effective cooling cycle allowed us to simulate the graph of the optical force that impinges the Barium atoms in function of their velocities.

Also, in the region of small velocities, we were able to extract the damping coefficient for each laser configuration, given the relation of linearity between the force and the velocity in this regime. Given the results from the simulation, all the 3 repumpers should be used to the cooling of the atoms, since the dynamics of the effective cooling cycle happens in a short time

scale, therefore, the cooling cycle must be closed with all the 3 repumpers.

In future work, an even further optimization of the lock-in of the laser frequency and, also, the experimental realization of a MOT setup, would both be a direct continuation of the research of the present work.

6

Appendix A: Output signal derivation in polarization spectroscopy

This derivation uses the reference [12]. Considering the probe beam as linearly polarized in the x direction, its decomposition is characterized as follows.

$$\vec{E}^{(+)}(z,t) = \frac{E_0}{2} e^{-i(\omega t - kz)} \vec{e}_x = \frac{E_0}{2\sqrt{2}} e^{-i(\omega t - kz)} \left(-\vec{\varepsilon}_+ + \vec{\varepsilon}_-\right) \tag{6.1}$$

Now, considering the definitions of n_{tot}, w_{tot}, n_+, n_-, ω_+, ω_-, Δn and $\Delta\omega$ given in the Section 2 **Theoretical Background**, we can describe the electric field after the interaction of the probe beam with the atomic medium in the HCL by the next expression.

$$\vec{E}_{out}^{(+)} = \frac{E_0}{2\sqrt{2}} \left(-\vec{\varepsilon}_+ e^{-i(\omega t - (n_+ + \omega_+)\frac{\omega}{c}L)} + \vec{\varepsilon}_- e^{-i(\omega t - (n_- + \omega_-)\frac{\omega}{c}L)}\right) \tag{6.2}$$

$$\vec{E}_{out}^{(+)} = \frac{E_0}{2\sqrt{2}} e^{-i(\omega t - (n_{tot} + \omega_{tot})\frac{\omega}{c}L)} \left(-\vec{\varepsilon}_+ e^{i(\Delta n + \Delta\omega)\frac{\omega}{2c}L)} + \vec{\varepsilon}_- e^{-i(\Delta n + \Delta\omega)\frac{\omega}{2c}L)}\right) \tag{6.3}$$

After the probe beam exits the HCL it goes through a Half-Wave Plate that has a fast axis which is rotated in relation to the x axis by an angle θ. This has an effect on the probe beam

given by the matrix below defined by the Jones approach [40].

$$\mathrm{M}(\theta) = -i \begin{pmatrix} \cos 2\theta & \sin 2\theta \\ \sin 2\theta & -\cos 2\theta \end{pmatrix} \tag{6.4}$$

Finally, the probe beam passes through a Polarizing Beam Splitter, in which it is decomposed into two components in the x and y directions. These components arrive in a balanced photodetector in two different channels. Therefore, the two components are given by the following relations.

$$\vec{E}_x^{(+)} = -i\frac{E_0}{4} e^{-i(\omega t - (n_{tot}+\omega_{tot})\frac{\omega}{c}L)} \left(e^{i2\theta} e^{i(\Delta n + \Delta\omega)\frac{\omega}{2c}L)} + e^{-i2\theta} e^{-i(\Delta n + \Delta\omega)\frac{\omega}{2c}L)} \right) \tag{6.5}$$

$$\vec{E}_y^{(+)} = -\frac{E_0}{4} e^{-i(\omega t - (n_{tot}+\omega_{tot})\frac{\omega}{c}L)} \left(e^{i2\theta} e^{i(\Delta n + \Delta\omega)\frac{\omega}{2c}L)} - e^{-i2\theta} e^{-i(\Delta n + \Delta\omega)\frac{\omega}{2c}L)} \right) \tag{6.6}$$

Now, considering that the balanced photodetector gives the difference of these two signals and that the intensity of the signal is $I \propto E^2$, the difference of intensity is given by the next expression.

$$\Delta I = \frac{E_0^2}{2} e^{-2Im(n_{tot}+\omega_{tot})\frac{\omega}{c}L} cos\left[Re(\Delta n + \Delta\omega)\frac{\omega}{c}L - 2\theta \right] \tag{6.7}$$

By considering $\theta = \frac{\pi}{4} + Re(\Delta\omega)\frac{\omega}{2c}L$ and that $Re(\Delta\omega)\frac{\omega}{2c}L << 1$, we obtain the Expression 2.59.

$$\Delta I = \frac{E_0^2}{2} Re(\Delta n) e^{-2Im(n_{tot}+\omega_{tot})\frac{\omega}{c}L} \frac{\omega}{c}L \tag{6.8}$$

Additionally, the angle θ can be obtained by changing the Half-Wave Plate position until the signal $\Delta I \approx 0$, since in this case $Re(\Delta n + \Delta\omega) \approx 0$ as well.

7

Appendix B: Difference of refractive index derivation

This derivation uses the references [12, 41] and, firstly, we consider that $\Omega_{probe} << \gamma_{12}$, therefore, the Expression 2.43 can be approximated as follows.

$$\chi = \frac{\Delta N}{V} \cdot \frac{|d_{12}|^2}{\hbar \varepsilon_0} \cdot \frac{1}{2} \cdot \frac{\delta + i\gamma_{12}}{\delta^2 + \gamma_{12}^2} \tag{7.1}$$

In this Expression 7.1, $\Delta N = N(\rho_{11}^0 - \rho_{22}^0)$, which is the population imbalance by taking into consideration only the pump beam (since the probe beam is weak in intensity). Given the saturation caused by the pump beam in the transition from $m = 0 \rightarrow m = +1$, there is a different value of the imbalanced population between the ground and excited states, given by the expressions below.

$$\Delta N^{(+)} = N\left(\rho_{11} - \rho_{22}^{(+)}\right) = N\left(1 - \frac{s}{s+1}\right) \tag{7.2}$$

$$\Delta N^{(-)} = N\left(\rho_{11} - \rho_{22}^{(-)}\right) = N\left(1 - \frac{1}{2}\frac{s}{s+1}\right) \tag{7.3}$$

Considering the expression for the saturation parameter 2.34, as well as the relations 7.1, 7.2 and 7.3, in addition to the inclusion of Doppler effects for both the pump and probe beams,

the difference of refractive indexes Δn is given below.

$$\Delta n = \frac{|d_{12}|^2}{2\hbar\varepsilon_0}\int \frac{dv}{\sqrt{2\pi v_{\text{th}}^2}} e^{-\frac{v^2}{2v_{\text{th}}^2}} \frac{1}{2}\cdot \frac{\delta - kv + i\gamma_{12}}{(\delta - kv)^2 + \gamma_{12}^2}\cdot \frac{\Delta n^{(+)} - \Delta n^{(-)}}{V} \tag{7.4}$$

$$\Delta n = -\frac{N}{V}\frac{|d_{12}|^2}{8\hbar\varepsilon_0}\int \frac{dv}{\sqrt{2\pi v_{\text{th}}^2}} e^{-\frac{v^2}{2v_{\text{th}}^2}} \cdot \frac{1}{(\delta - kv) - i\gamma_{12}}\cdot \frac{\frac{\Omega^2 2\gamma_{12}}{2\Gamma_{12}}}{(\delta + kv)^2 + \gamma_s^2} \tag{7.5}$$

Due to the characteristic large time scale of variation of the Gaussian part of the Expression 7.5 above, it is possible to approximate it as constant and perform an integration with relation to the other parts with a residual theorem procedure. In this case, there are three poles, which are $\delta - i\gamma_{12}$, $-\delta - i\gamma_s$ and $-\delta + i\gamma_s$, in which the last one has a positive imaginary term. By doing the integral with a closed path around this third pole, after the rapid convergence, Δn becomes the following.

$$\Delta n = -\frac{N}{V}\frac{|d_{12}|^2}{8\hbar\varepsilon_0}\frac{e^{-\frac{\delta^2}{2(kv_{\text{th}})^2}}}{\sqrt{2\pi}kv_{\text{th}}}\cdot \frac{1}{2\delta - i(\gamma_{12} + \gamma_s)}\cdot \frac{\frac{2\pi i\Omega^2 2\gamma_{12}}{2\Gamma_{12}}}{2i\gamma_s} \tag{7.6}$$

$$\Delta n = -\frac{N}{V}\frac{|d_{12}|^2}{8\hbar\varepsilon_0}\frac{\Omega^2\gamma_{12}}{2\Gamma_{12}}\frac{\pi e^{-\frac{\delta^2}{2(kv_{\text{th}})^2}}}{\sqrt{2\pi}kv_{\text{th}}\gamma_s}\cdot \frac{\delta + i\frac{(\gamma_{12}+\gamma_s)}{2}}{\delta^2 + \frac{(\gamma_{12}+\gamma_s)^2}{4}} \tag{7.7}$$

Consequently, the real part of the difference of the refractive indexes is given below and it is precisely the Expression 2.60, which is now properly derived.

$$\Delta n = -\frac{N}{V}\frac{|d_{12}|^2}{8\hbar\varepsilon_0}\frac{\Omega^2\gamma_{12}}{2\Gamma_{12}}\frac{\pi e^{-\frac{\delta^2}{2(kv_{\text{th}})^2}}}{\sqrt{2\pi}kv_{\text{th}}\gamma_s}\cdot \frac{\delta}{\delta^2 + \frac{(\gamma_{12}+\gamma_s)^2}{4}} \tag{7.8}$$

References

[1] A. Bayerstadler, G. Becquin, J. Binder, T. Botter, H. Ehm, T. Ehmer, M. Erdmann, N. Gaus, P. Harbach, M. Hess *et al.*, "Industry quantum computing applications," *EPJ Quantum Technology*, vol. 8, no. 1, p. 25, 2021.

[2] S. K. Sood *et al.*, "Quantum computing review: A decade of research," *IEEE Transactions on Engineering Management*, vol. 71, pp. 6662–6676, 2023.

[3] C. D. Bruzewicz, J. Chiaverini, R. McConnell, and J. M. Sage, "Trapped-ion quantum computing: Progress and challenges," *Applied physics reviews*, vol. 6, no. 2, 2019.

[4] E. Peik, T. Schneider, and C. Tamm, "Laser frequency stabilization to a single ion," *Journal of Physics B: Atomic, Molecular and Optical Physics*, vol. 39, no. 1, p. 145, 2005.

[5] M. R. Dietrich, A. Avril, R. Bowler, N. Kurz, J. S. Salacka, G. Shu, and B. B. Blinov, "Barium ions for quantum computation," 2009. [Online]. Available: https://arxiv.org/abs/0905.2701

[6] H. Wang, Y. Lei, Q. Cui, S. Li, X. Song, Y. Chen, L. Liang, P. Jia, C. Qiu, Y. Song *et al.*, "Noise characteristics of semiconductor lasers with narrow linewidth," *Heliyon*, vol. 10, no. 20, 2024.

[7] G. Kirchmair, *Frequency stabilization of a Titanium-Sapphire laser for precision spectroscopy on Calcium ions*. na, 2006.

[8] N. I. of Standards and T. (NIST), "Basic atomic spectroscopy data - barium (ba)," https://physics.nist.gov/PhysRefData/Handbook/Tables/bariumtable1.htm, 2025, accessed: 2025-02-20.

[9] S. De, U. Dammalapati, K. Jungmann, and L. Willmann, "Magneto-optical trapping of barium," *Physical Review A—Atomic, Molecular, and Optical Physics*, vol. 79, no. 4, p. 041402, 2009.

[10] Z. et al., "Magnetic properties and the zeeman effect," n.d., accessed: 2025-02-23. [Online]. Available: https://chem.libretexts.org/Bookshelves/Physical_and_Theoretical_Chemistry_Textbook_Maps/Book%3A_Quantum_States_of_Atoms_and_Molecules_%28Zielinksi_et_al%29/08%3A_The_Hydrogen_Atom/8.04%3A_Magnetic_Properties_and_the_Zeeman_Effect

[11] M. S. Suzuki, "Selection rule for electric dipole transition," 2014, accessed: 2025-02-24. [Online]. Available: https://bingweb.binghamton.edu/~suzuki/QuantumMechanicsFiles/2-2_Selection_rule_for_electric_dipole_transition.pdf

[12] L. Pagot, "Laser frequency stabilization in a calcium optogalvanic lamp," Master's thesis, ETH Zürich, Zurich, Switzerland, 2023, supervised by W. Adamczyk and Dr. H. Fernandes Passagem, Group leader: Prof. Dr. J. Home. [Online]. Available: https://ethz.ch/content/dam/ethz/special-interest/phys/quantum-electronics/tiqi-dam/documents/masters_theses/masterthesis-Louis-Pagot

[13] C. Cohen-Tannoudji, J. Dupont-Roc, and G. Grynberg, *Photons and atoms: introduction to quantum electrodynamics*. John Wiley & Sons, 2024.

[14] G. Grynberg, A. Aspect, and C. Fabre, *Introduction to quantum optics: from the semi-classical approach to quantized light*. Cambridge university press, 2010.

[15] F. Lindenfelser, "Broadband cooling on a forbidden transition in a novel high-optical-access ion trap," Ph.D. dissertation, ETH Zurich, 2017.

[16] H. Oberst, *Resonance fluorescence of single barium ions*. na, 1999.

[17] S. De, U. Dammalapati, and L. Willmann, "Lifetime determination of the 5 d 2 3 f 2 state in barium using trapped atoms," *Physical Review A*, vol. 91, no. 3, p. 032517, 2015.

[18] C. J. Foot, *Atomic physics*. Oxford university press, 2005, vol. 7.

[19] D. L. Andrews, "Laser spectroscopy 1: Basic principles & laser spectroscopy 2: Experimental techniques scope: handbook, monograph, reference, text book. level: postgraduate, early career researcher, researcher, teacher, specialist, scientist, engineers." *Contemporary Physics*, vol. 56, no. 4, pp. 487–488, 2015.

[20] C. Wieman and T. W. Hänsch, "Doppler-free laser polarization spectroscopy," *Physical Review Letters*, vol. 36, no. 20, p. 1170, 1976.

[21] M. Mills, P. Puri, Y. Yu, A. Derevianko, C. Schneider, and E. R. Hudson, "Efficient repumping of a ca magneto-optical trap," *Physical Review A*, vol. 96, no. 3, p. 033402, 2017.

[22] S. Eckel, D. S. Barker, E. B. Norrgard, and J. Scherschligt, "Pylcp: A python package for computing laser cooling physics," *Computer physics communications*, vol. 270, p. 108166, 2022.

[23] B. Baragiola and contributors, "1d mot forces: F=0 to f'=1," https://python-laser-cooling-physics.readthedocs.io/en/latest/examples/MOTs/00_F0_to_F1_1D_MOT_forces.html, 2023, accessed: 2025-06-23. [Online]. Available: https://python-laser-cooling-physics.readthedocs.io/en/latest/examples/MOTs/00_F0_to_F1_1D_MOT_forces.html

[24] Alexander Franzen, Gravitational Wave Optics Group, "Component library," https://www.gwoptics.org/ComponentLibrary/, 2006, accessed: 2025-04-22.

[25] R. P. Team, "Red pitaya quick start guide," https://redpitaya.readthedocs.io/en/latest/quickStart/first.html, 2025, accessed: 2025-04-25.

[26] S. R. Systems, "About lock-in amplifiers," Dec. 2022, accessed: 2025-04-26.

[27] D. J. McCarron, "A guide to acousto-optic modulators," *Интернет: http://massey. dur. ac. uk/resources/slcornish/AOMGuide. pdf*, 2007.

[28] D. Nadlinger, "Laser intensity stabilization and pulse shaping for trapped-ion experiments using acousto-optic modulators," 2014, accessed: 2025-05-25. [Online]. Available: https://ethz.ch/content/dam/ethz/special-interest/phys/quantum-electronics/tiqi-dam/documents/semester_theses/semesterthesis-david_nadlinger.pdf

[29] K. Brodie and S. Neate, "Features and operation of hollow cathode lamps and deuterium lamps," *Varian Instruments At Work, AA-83*, 1988.

[30] M. S. H. Akash and K. Rehman, "Atomic absorption spectroscopy," in *Essentials of Pharmaceutical Analysis*, ser. Essentials of Pharmaceutical Analysis. Singapore: Springer, 2020, pp. 85–102. [Online]. Available: https://link.springer.com/chapter/10.1007/978-981-15-1547-7_6

[31] M. Guina, A. Rantamäki, and A. Härkönen, "Optically pumped vecsels: review of technology and progress," *Journal of Physics D: Applied Physics*, vol. 50, no. 38, p. 383001, 2017.

[32] Vexlum Ltd, "Vexsel technology," https://vexlum.com/technology/, Tampere, Finland, 2025, accessed: 2025-06-01. [Online]. Available: https://vexlum.com/technology/

[33] E. Kantola, J.-P. Penttinen, S. Ranta, and M. Guina, "72-w vertical-external-cavity surface-emitting laser with 1180-nm emission for laser guide star adaptive optics," *Electronics Letters*, vol. 54, no. 19, pp. 1135–1137, 2018.

[34] A. Kramida, Y. Ralchenko, J. Reader, and NIST ASD Team, "NIST Atomic Spectra Database (ver. 5.10), [Ba I lines 553.2–553.9 nm]," https://physics.nist.gov/asd, 2024, national Institute of Standards and Technology, Gaithersburg, MD.

[35] M. González-Cardel, P. Arguijo, and R. Díaz-Uribe, "Gaussian beam radius measurement with a knife-edge: a polynomial approximation to the inverse error function," *Applied optics*, vol. 52, no. 16, pp. 3849–3855, 2013.

[36] A. E. Siegman, *Lasers*. University science books, 1986.

[37] D. A. Steck, "Rubidium 87 d line data," 2001.

[38] Santec, "mw to dbm conversion calculator," https://inst.santec.com/mw-to-dbm-conversion-calculator, 2025, accessed: 2025-06-21.

[39] B. Wiegand, B. Leykauf, R. Jördens, and M. Krutzik, "Linien: A versatile, user-friendly, open-source fpga-based tool for frequency stabilization and spectroscopy parameter optimization," *Review of Scientific Instruments*, vol. 93, 6 2022.

[40] R. C. Jones, "A new calculus for the treatment of optical systems i. description and discussion of the calculus," *Journal of the Optical Society of America*, vol. 31, no. 7, pp. 488–493, 1941.

[41] M. Levenson, *Introduction to Nonlinear Laser Spectroscopy 2e*. Elsevier, 2012.